A State-dependent Error Covariance Model of Surface Atmospheric Forcings over the Arctic Sea Ice

Hee-Sung Jung,[a] Jonathan Poterjoy,[a] and Alek Petty[b]

[a] *Department of Atmospheric and Oceanic Science, University of Maryland, College Park, Maryland, USA*

[b] *Earth System Science Interdisciplinary Center (ESSIC), University of Maryland, College Park, Maryland, USA*

Corresponding author: Hee-Sung Jung, hsjung24@umd.edu

ABSTRACT: This paper presents a state-dependent error covariance model of surface atmospheric forcings over Arctic sea ice for constraining atmospheric influences on short-range sea ice forecast errors. Atmospheric influences are argued to be a dominant source of sea ice forecast errors at shorter lead times and thus need to be properly accounted for in generating ensemble sea ice forecasts relevant for operational assimilation systems. The proposed covariance model is built on ensemble perturbations from 10 years of an 80-member atmospheric reanalysis using methods adapted from background error covariance modeling. Specifically, the covariance model consists of a set of matrix operators that each encodes the inter-variable relationships (i.e., balance operators) and the spatiotemporal correlation structures. Comparison of statistics of perturbations from the covariance model with statistics of ensemble perturbations from an atmospheric reanalysis over the validation period reveal good agreement. In particular, balance relationships that are highly state-dependent, such as temperature-humidity balance, are well captured within the error covariance model. Perfect model experiments using the Los Alamos sea ice model (CICE5) show that an atmospheric forcing ensemble generated from the error covariance model can replicate the atmospheric influences on sea ice ensemble forecasts observed when using a reanalysis atmospheric forcing ensemble. These experiments also demonstrate the ability of the covariance model for introducing controllable amounts of forcing error within the sea ice forecast while properly quantifying the error in the ensemble statistics, which can be useful for generating Observing System Simulation Experiments (OSSEs) targeting short-range forecasts.

1. Introduction

Global weather prediction systems are increasingly incorporating a dynamic sea ice model due to its advantages over persistent sea ice in enhancing short-range (i.e., couple of hours to days) forecast skill (Keeley and Mogensen 2018; Barton et al. 2021; Peterson et al. 2022). These forecast enhancements include improvements in near-surface temperature and humidity, especially in regions of high sea ice variability, such as the marginal ice zone, Arctic cyclone tracks, and summer Arctic sea ice (Parkinson and Comiso 2013; Day et al. 2022; Wang et al. 2020; Cavallo et al. 2025; Croad et al. 2025).

To maintain realistic sea ice and associated atmosphere/ocean states throughout the model forecast, sea ice data assimilation (DA) has become an increasing focus. Various aspects of sea ice DA have been explored in recent years to better understand the impact and methods for reliably assimilating sea ice observations (Zhang et al. 2018, 2021; Fiedler et al. 2022; Mignac et al. 2022; Lee and Ham 2022; Williams et al. 2023; Riedel and Anderson 2024; Wieringa et al. 2024; Riedel et al. 2025). These DA experiments have been performed both in real-world and perfect model settings. The latter, which is constructed by assuming a reference model simulation is the truth (i.e., nature run), is a popular experimental framework due to the benefits in interpretation of imposing a known truth. There is also the flexibility to simulate various types of observations, which is useful for testing capabilities of hypothetical/future observations in constraining the sea ice model state (i.e., Observing System Simulation Experiment; OSSE).

An important prerequisite for any DA experiment is a precise estimate of forecast uncertainty. In particular, Kalman filter-based DA methods rely on these uncertainty estimates, in the form of error covariance, to form the best linear unbiased estimate (BLUE) of the model state given observations, typically referred to as an analysis. For this purpose, the forecast uncertainty helps assess the relative contribution of observations to the analysis, thus directly factoring into the quality of the subsequent forecasts (Mathiot et al. 2012; Blayo et al. 2014; Guemas et al. 2016; Tian et al. 2021).

A common approach for estimating forecast uncertainty is to use statistics derived from an ensemble of model forecasts, which provides a Monte-Carlo estimate of the forecast error distribution (Leutbecher and Palmer 2008). However, for sea ice models, obtaining an ensemble that faithfully represents all sources of forecast error is difficult because errors in sea ice forecasts are not

self-contained, but are influenced by errors from other components of the Earth system, primarily the atmosphere and ocean. For short-range forecasts in particular (i.e., on time scales of hours to days), the atmospheric influence is argued to be one of the dominant drivers of forecast errors in sea ice (Evensen 2003; Yang et al. 2015; Mohammadi-Aragh et al. 2018).

Coupled Earth System Models (ESMs) provide a means of accounting for atmospheric/oceanic influences on sea ice forecast errors, which can be achieved by running an ensemble of forecasts for the entire set of model components (Kay et al. 2015; Simpson et al. 2023). However, running an ensemble forecast using a fully coupled ESM is not always possible due to limitations in computational power and storage. Additional challenges arise when the focus shifts to errors associated with shorter forecast lead times. When using an ensemble to quantify such errors, there is a need to constrain the ensemble to remain representative of the shorter time scale. This can be achieved by periodically re-initializing the model with initial conditions that have been improved by DA, from which an ensemble of hindcasts can be run for the lead time of interest to quantify the forecast errors (Parrish and Derber 1992; Fisher 2003). Although advances have been made in performing DA with a coupled ESM, technical and scientific challenges remain, such as accounting for model errors associated with the coupling process and using interface observations that depend on multiple components of the ESM (Penny et al. 2019; Tang et al. 2021; de Rosnay et al. 2022; Valmassoi et al. 2023; Schüller et al. 2025; Kousal et al. 2025).

For sea ice, the compromise often made to reduce computational effort is to run only the sea ice model in a forced/standalone configuration. The remaining ESM components, mostly the atmosphere and/or ocean, then act as a forcing. In the standalone configuration, forcing errors are typically represented by using an ensemble of atmosphere/ocean reanalysis data as forcings (Zhang et al. 2018; Riedel and Anderson 2024). However, using a reanalysis has limitations in that the forcing errors and its ensemble representation within the sea ice forecasts become tailored to that of the reanalysis product. In the context of DA, this lack of control over the forcing uncertainty means that an incorrect representation of forecast uncertainty from the ensembles (i.e., over/under-disperse ensemble) cannot be readily corrected, which can limit the performance of the DA system and consequently degrade the forecast quality (Palmer et al. 2006; Harlim and Majda 2010; Rodwell et al. 2016). Additional inconveniences exist, such as the experiments being

confined to the reanalysis period, fixed DA schedules from the reanalysis, and the often limited ensemble size provided in reanalysis outputs.

To address the above limitations, past studies have explored strategies that induce a controllable amount of uncertainty in forcings (Evensen 2003; Cheng et al. 2023; Williams et al. 2023; Xie et al. 2026). In this approach, an ensemble of forcings is created by perturbing a deterministic forcing. This ensemble can then be easily adjusted to accommodate the needs of the DA system by changing the distribution from which the perturbations are sampled, providing more flexibility in tuning the resultant sea ice ensemble. There is also no constraint on the experimental period or the ensemble size since the forcing ensemble is now generated from a perturbation model.

However, obtaining a realistic distribution of forcing errors is not a trivial task, since the forcings are typically of high dimension with complex correlation structures. The distribution of forcing errors is also known to be highly state-dependent and vary with both the diurnal and seasonal cycles. These complexities, which are automatically encoded within a reanalysis ensemble via a dynamical model, need to be manually prescribed within the perturbation model to produce an accurate analog of the actual forcing errors. Existing atmospheric forcing error models typically simplify the underlying error distribution by neglecting some combination of spatial, temporal, cross-variable dependencies (Brusdal et al. 2003; Turner et al. 2008; Mirouze and Storto 2019). While recent multivariate EOF-based approaches have successfully represented multivariate and spatiotemporal correlations, they assume a stationary error distribution that does not vary with season or time of day (TOD) (Zheng and Zhu 2008; Luo et al. 2023).

In this study, we aim to extend on the idea of using a perturbation model to represent atmospheric forcing errors in sea ice forecasting. We relax some simplifying assumptions made in previous efforts, by adopting classical methods of background error covariance modeling that have emerged from the variational DA community for representing state, diurnal, and seasonal error dependence. The atmospheric forcing errors that we target are those associated with short-range atmosphere/sea ice forecasts. This is for two main reasons: First, as mentioned previously, the relevance of short-range sea ice forecast errors is a primary concern with operational centers incorporating dynamical sea ice components, and the impacts extend to the entire global weather prediction system. Therefore, it is desirable to have control over the dominant driver of such errors, which is the atmospheric forcing error. Second, although not in this paper, we intend to create OSSEs

to inform the various challenges of operational sea ice DA associated with short-range forecast skill. Since the characteristic of atmospheric forcing errors can vary with the timescale of interest, a perturbation model trained specifically for timescales associated with short-range forecasts is needed for creating realistic OSSEs.

The manuscript is organized as follows: Section 2 presents the data used to train/validate our error covariance model. Section 3 presents the methods used to encode the correlation structures in our error covariance model. Section 4 illustrates key properties of our error covariance model from the sample statistics. Section 5 shows the application of our error covariance model to prescribe forcing errors in a sea ice ensemble forecast. Section 6 presents the conclusion.

2. Training and validation data

In this study, we use atmospheric reanalysis data produced by Raeder et al. (2021) to train and validate the error covariance model. The reanalysis are from a 6-hourly cycling DA system, with analyses produced at 0, 6, 12, and 18 UTC each day. The reanalysis uses the Community Atmospheric Model version 6 (CAM6) coupled with the Data Assimilation Research Testbed (DART) within the Community Earth System Model version 2 (CESM2) framework (Danabasoglu et al. 2020; Gharamti et al. 2025). Forcing data are provided as 80-member forecasts from the reanalysis ensemble, averaged over the first 3-h of integration, that span 10 years (2011–2020) with a spatial resolution of approximately 1° latitude/longitude. In this study, we focus on an Arctic domain; i.e., all regions above $40°N$. To account for seasonal and diurnal cycles in the atmospheric forcing errors, the reanalysis dataset is stratified according to the month and the TOD. Thus, a total of 96 error covariance models (i.e., 12 months × 8 TODs) are trained, which are expressed as:

$$\hat{P} = \{\hat{\mathbf{P}}_{\text{month,time}} \mid \text{month} = 1, 2, ..., 12; \text{time} = (0,3), (3,6), ..., (21,0)\ \text{UTC}\}, \tag{1}$$

where the hat sign denotes modeled error covariance. By allowing the covariance model to vary periodically in time, we relax the assumption of a stationary process implied in many previous covariance modeling studies and attempt to resolve seasonal and diurnal dependence of the atmospheric forcing error distribution.

In this study, data from years 2011 to 2018 are used to train the covariance model, while years 2019 and 2020 are reserved for validation. In the following section, the training process for each

element of $\hat{P}$ is illustrated, so unless explicitly noted, the subscripts for the month and the TOD are dropped. It is worth noting that due to 3-hourly averaging of the training data, the error covariance will learn forecast errors averaged over select time windows. Using 3-hourly averaged fields instead of instantaneous fields has benefits for assessing multivariate relationships, such as those between wind and mass fields, since it acts to low-pass filter the data, allowing for the analysis of perturbations that have had time to reach a balanced state (Honda et al. 2006).

3. Error covariance model

a. Notations

We define the atmospheric forcing as an N-dimensional vector that contains 13 atmospheric variables (see Table A1) at K grid points within the study domain shown by:

$$\boldsymbol{\psi} = \begin{bmatrix} \boldsymbol{\psi}^1 \\ \boldsymbol{\psi}^2 \\ \vdots \\ \boldsymbol{\psi}^{13} \end{bmatrix} \in \mathbb{R}^{N=13\times K}, \tag{2}$$

where $\boldsymbol{\psi}^i \in \mathbb{R}^K$ refers to the i^{th} variable. Variables associated with precipitation are not included in $\boldsymbol{\psi}$ due to their highly non-Gaussian nature. The drawbacks of not perturbing precipitation are discussed in Section 5. The training dataset for a covariance model for a given month and TOD is a subset of the full training dataset shown by:

$$\{\boldsymbol{\psi}\} = \{\boldsymbol{\psi}_{t,m} \mid t = 1, 2, ..., T; m = 1, 2, ..., M\}, \tag{3}$$

where T and M are the number of available time steps and the number of ensemble members, respectively. The ensemble means and error covariances of $\boldsymbol{\psi}$ are computed as:

$$\{\bar{\boldsymbol{\psi}}\} = \{\bar{\boldsymbol{\psi}}_t = \frac{1}{M}\sum_{m=1}^{M} \boldsymbol{\psi}_{t,m} \mid t = 1, 2, .., T\}, \tag{4}$$

$$\{\hat{\boldsymbol{p}}\} = \{\hat{\boldsymbol{p}}_t = \frac{1}{M-1}\sum_{m=1}^{M}(\boldsymbol{\psi}_{t,m} - \bar{\boldsymbol{\psi}}_t)(\boldsymbol{\psi}_{t,m} - \bar{\boldsymbol{\psi}}_t)^T \mid t = 1, 2, ..., T\}. \quad (5)$$

Here, the departure of individual members from the ensemble mean ($\boldsymbol{\psi}'_{t,m} = \boldsymbol{\psi}_{t,m} - \bar{\boldsymbol{\psi}}_t$) have been used as proxies of the atmospheric forcing error in estimating the error covariance (Fisher 2003; Caya et al. 2010). It is noted that model errors are not accounted for in $\boldsymbol{\psi}'$ as all members use the same atmospheric model. The climatological value of the error covariance can be estimated by taking the average of $\hat{\boldsymbol{p}}_t$ within the subset, which is shown by:

$$\hat{\mathbf{P}} = \frac{1}{T}\sum_{t=1}^{T}\hat{\boldsymbol{p}}_t. \quad (6)$$

The large dimension of $\boldsymbol{\psi}$ (on the order of 10^5) prohibits direct use of $\hat{\mathbf{P}}$ for sampling errors, which requires diagonalizing $\hat{\mathbf{P}}$, computationally unfeasible. Methods to approximate the diagonalization of a large matrix have been developed to model the background error covariance in variational DA (i.e., control variable transform; Parrish and Derber 1992; Derber and Bouttier 1999; Lorenc et al. 2000; Wu et al. 2002; Bannister 2008). Control variable transform can be divided into the following two steps: (1) modeling inter-variable correlation and (2) modeling spatial correlation. In this study, these steps, along with an additional step to prescribe temporal correlations, are applied to model $\hat{\mathbf{P}}$.

b. Balance operator

$\hat{\mathbf{P}}$ can be expressed block-wise as:

$$\hat{\mathbf{P}} = \begin{bmatrix} \mathbf{p}_{1,1} & \mathbf{p}_{1,2} & \cdots & \mathbf{p}_{1,13} \\ \mathbf{p}_{2,1} & \mathbf{p}_{2,2} & \cdots & \mathbf{p}_{2,13} \\ \cdots & & & \\ \mathbf{p}_{13,1} & \mathbf{p}_{13,2} & \cdots & \mathbf{p}_{13,13} \end{bmatrix}. \quad (7)$$

Here, each sub-matrix $\mathbf{p}_{i,j} \in \mathbb{R}^{K\times K}$ is the covariance between the i^{th} and the j^{th} variable. Thus, modeling inter-variable correlation is equivalent to finding a transformation that makes $\hat{\mathbf{P}}$ block-diagonal.

We do this by defining a matrix $\mathbf{K}$, often referred to as the balance operator, that partitions the error into a sum of balanced (i.e., the portion of perturbation that is correlated with perturbations of other variables) and unbalanced components as the following:

$$\boldsymbol{\psi}' = \boldsymbol{\psi}'^{b} + \boldsymbol{\psi}'^{ub} = \mathbf{K}\boldsymbol{\psi}'^{ub}, \tag{8}$$

where $\boldsymbol{\psi}'^{b}$ and $\boldsymbol{\psi}'^{ub}$ denote the balanced and unbalanced components of $\boldsymbol{\psi}'$, respectively (Derber and Bouttier 1999; Weaver et al. 2006). The balance operator we propose is a lower triangular matrix shown by:

$$\begin{bmatrix} \mathbf{p}' \\ \boldsymbol{\theta}' \\ \ln(\mathbf{q})' \\ \mathbf{u}' \\ \mathbf{v}' \\ \mathbf{F}'_{lw} \\ \mathbf{F}'_{nr} \\ \mathbf{F}'_{vr} \\ \mathbf{F}'_{nf} \\ \mathbf{F}'_{vf} \end{bmatrix} = \begin{bmatrix} \mathbf{I} & \mathbf{0} & \mathbf{0} & \mathbf{0} & \mathbf{0} & \mathbf{0} & \mathbf{0} & \mathbf{0} & \mathbf{0} & \mathbf{0} \\ \mathbf{0} & \mathbf{I} & \mathbf{0} & \mathbf{0} & \mathbf{0} & \mathbf{0} & \mathbf{0} & \mathbf{0} & \mathbf{0} & \mathbf{0} \\ \mathbf{k}_{q,p} & \mathbf{k}_{q,\theta} & \mathbf{I} & \mathbf{0} & \mathbf{0} & \mathbf{0} & \mathbf{0} & \mathbf{0} & \mathbf{0} & \mathbf{0} \\ \mathbf{k}_{u,p} & \mathbf{k}_{u,z}\mathbf{k}_{z,\theta} & \mathbf{k}_{u,z}\mathbf{k}_{z,q} & \mathbf{I} & \mathbf{0} & \mathbf{0} & \mathbf{0} & \mathbf{0} & \mathbf{0} & \mathbf{0} \\ \mathbf{k}_{v,p} & \mathbf{k}_{v,z}\mathbf{k}_{z,\theta} & \mathbf{k}_{v,z}\mathbf{k}_{z,q} & \mathbf{0} & \mathbf{I} & \mathbf{0} & \mathbf{0} & \mathbf{0} & \mathbf{0} & \mathbf{0} \\ \mathbf{0} & \mathbf{0} & \mathbf{0} & \mathbf{0} & \mathbf{0} & \mathbf{k}_{lw} & \mathbf{0} & \mathbf{0} & \mathbf{0} & \mathbf{0} \\ \mathbf{0} & \mathbf{0} & \mathbf{0} & \mathbf{0} & \mathbf{0} & \mathbf{k}_{nr,lw} & \mathbf{k}_{nr} & \mathbf{0} & \mathbf{0} & \mathbf{0} \\ \mathbf{0} & \mathbf{0} & \mathbf{0} & \mathbf{0} & \mathbf{0} & \mathbf{k}_{vr,lw} & \mathbf{k}_{vr,nr} & \mathbf{k}_{vr} & \mathbf{0} & \mathbf{0} \\ \mathbf{0} & \mathbf{0} & \mathbf{0} & \mathbf{0} & \mathbf{0} & \mathbf{k}_{nf,lw} & \mathbf{k}_{nf,nr} & \mathbf{k}_{nf,vr} & \mathbf{k}_{nf} & \mathbf{0} \\ \mathbf{0} & \mathbf{0} & \mathbf{0} & \mathbf{0} & \mathbf{0} & \mathbf{k}_{vf,lw} & \mathbf{k}_{vf,nr} & \mathbf{k}_{vf,vr} & \mathbf{k}_{vf,nf} & \mathbf{k}_{vf} \end{bmatrix} \begin{bmatrix} \mathbf{p}'^{ub} \\ \boldsymbol{\theta}'^{ub} \\ \ln(\mathbf{q})'^{ub} \\ \mathbf{u}'^{ub} \\ \mathbf{v}'^{ub} \\ \mathbf{F}'^{ub}_{lw} \\ \mathbf{F}'^{ub}_{nr} \\ \mathbf{F}'^{ub}_{vr} \\ \mathbf{F}'^{ub}_{nf} \\ \mathbf{F}'^{ub}_{vf} \end{bmatrix}. \tag{9}$$

Here, sub-matrices $\mathbf{k} \in \mathbb{R}^{K \times K}$ are diagonal matrices with elements containing the balance coefficient evaluated at the model grid-points. The balance coefficients in Eq. 9 are estimated using a combination of analytical and statistical methods, which are further described in the subsequent sections.

1) Diagnostic variables

CAM6, along with many global atmospheric models, uses a hybrid-sigma vertical coordinate system (Phillips 1957; Kasahara 1974). In particular, the atmospheric forcings in CAM6 are

provided at the lowest model level at which the vertical coordinate is:

$$\sigma_0 = \frac{p}{p_s}, \tag{10}$$

where p_s is the surface pressure and σ_0 is a constant value representing the vertical coordinate. Due to this characteristic, perturbations in T, z, and ρ can be diagnosed from other thermodynamic variables. First, the definition of potential temperature can be used to diagnose temperature perturbations:

$$T'^b = \left(\frac{p}{p_s}\right)^{\kappa} \theta' = \sigma_0^{\kappa}\theta' = \Pi\theta', \tag{11}$$

where the Exner function $\Pi = \sigma_0^{\kappa}$ becomes a constant since σ_0 is a fixed at the lowest model level and $\kappa = \frac{R_d}{C_p}$. Next, the hypsometric equation relates z' to θ' according to:

$$z'^b \approx \left[-\frac{R_d}{g}\ln(\sigma_o)\Pi\left(1 + \frac{1-\epsilon}{\epsilon}\bar{q}\right)\right]\theta' + \left[-\frac{R_d}{g}\ln(\sigma_o)\Pi\left(\frac{1-\epsilon}{\epsilon}\right)\bar{\theta}\right]q' = k_{z,\theta}\theta' + k_{z,q}q', \tag{12}$$

where $\epsilon = \frac{R_d}{R_v}$ and $k_{z,\theta}$ and $k_{z,q}$ constitute the diagonals of $\mathbf{k}_{z,\theta}$ and $\mathbf{k}_{z,q}$ in Eq. 9. The approximation denotes that we have assumed constant temperature/humidity profiles when integrating the hydrostatic equation to obtain Eq. 12 (see Appendix B for details). Similarly, the ideal gas law can be linearized to relate ρ' to p', θ', and q' according to:

$$\rho'^b = \left[\frac{1}{R_d\left(1 + \frac{1-\epsilon}{\epsilon}\bar{q}\right)\Pi\bar{\theta}}\right]P' + \left[-\frac{\bar{p}}{R_d\left(1 + \frac{1-\epsilon}{\epsilon}\bar{q}\right)\Pi\bar{\theta}^2}\right]\theta' + \left[-\frac{\frac{1-\epsilon}{\epsilon}\bar{p}}{R_d\left(1 + \frac{1-\epsilon}{\epsilon}\bar{q}\right)^2\Pi\bar{\theta}}\right]q'. \tag{13}$$

Linear correlations between the balanced and full components of T', z', and ρ' all exceed 0.99 (not shown), supporting the decision to make the three variables fully diagnostic.

2) Specific humidity balance

Specific humidity balance is modeled as the sum of a local thermodynamic component and a non-local component. The local thermodynamic component is derived by linearizing the following equation:

$$q \approx \frac{\epsilon e}{p}, \tag{14}$$

where, e is the vapor pressure and we have approximated $p + e \approx p$ in the denominator (Holm et al. 2002; Ingleby et al. 2013). Taking the logarithm of Eq. 14, linearization is performed conditionally on the mean state's closeness to saturation, which is shown as:

$$(\ln q)'_{local} \approx \begin{cases} \left[-\frac{1}{\bar{p}}\right] p' + \left[\Pi \frac{d \ln e_s}{dT}\Big|_{\bar{T}}\right] \theta' & \text{(Close to saturation)} \\ \left[-\frac{1}{\bar{p}}\right] p' & \text{(Far from saturation)} \end{cases}. \tag{15}$$

Here, $\frac{d \ln e_s}{dT}$ is evaluated from the Goff-Gratch formula for saturation vapor pressure over liquid for $T > 273.16K$ and over solid for $T \leq 273.16K$ (Goff and Gratch 1946; Ingleby et al. 2013). In this study, the mean state is considered close to saturation if a temperature perturbation of one standard deviation obtained from the training data subset leads to saturation.

Removing the local thermodynamic component, i.e., $(\ln q)'_{local}$, reveals systematic correlations between θ' and the residual specific humidity, $(\ln q)' - (\ln q)'_{local}$, indicating the presence of non-local coupling mechanisms. Figure 1 illustrates these relationships through grid-point-wise correlation maps. In saturated regions (green contours in Fig. 1a), strong positive correlations between θ' and $(\ln q)'$ are consistent with the local thermodynamic balance described by Eq. 15. Correlations between θ' and $(\ln q)'$ weaken in sub-saturated regions (blue contours in Fig. 1a), however, do not tend towards zero, confirming that local thermodynamics does not explain the full balance.

The existence of non-local balance is evident in Fig. 1b, which shows the correlation map between θ' and $(\ln q)' - (\ln q)'_{local}$. The correlations show clear spatial patterns: negative correlations over land/ice surfaces and positive correlations over sub-saturated ocean surfaces. One contributing mechanism arises from the use of sigma coordinates in the CAM6 forcing fields. A positive temperature perturbation raises the geometric height of a constant-sigma surface, sampling air with lower background humidity and producing a negative q'–θ' correlation (Li et al. 2023). A second mechanism involves surface moisture fluxes: near the surface, warming increases atmospheric moisture demand, enhancing evaporation and generating a positive q'–θ' correlation even under unsaturated conditions. These competing effects likely explain the contrasting land and ocean patterns, with limited evaporation over land and ice allowing the vertical-coordinate effect to dominate, while stronger ocean evaporation offsets or exceeds it. Additional contributions from

moisture advection and turbulent mixing may also influence the residual humidity field (Raymond 2000; McColl and Tang 2024; Shakespeare and Roderick 2024).

In this study, we refer to the combined effects of the processes mentioned above as non-local balance and model it by grid-point-wise linear regression with $(\ln q)' - (\ln q)'_{local}$ as the response variable and θ' as the predictor shown as:

$$(\ln q)'_{non-local} = \widehat{(\ln q)' - (\ln q)'_{local}} = \beta\theta', \tag{16}$$

where, β is the regression coefficient. β is estimated conditionally on the mean state's closeness to saturation and on the surface type; i.e., open ocean, land, or sea ice. This is achieved by stratifying the samples into a total of 6 (2 saturation criterion $\times$ 3 surface type criterion) bins and estimating β's from the stratified samples. β is only estimated when at a given grid-point and bin there are more than 80 samples available. If there are not enough samples to give an estimate of β, the average value of βs collected about a $\pm 5^\circ$ latitude band from the current grid-point corresponding to the same bin is used to fill in the missing values. We find that interpolated values of β are rarely used when tested over the validation data.

The final form of specific humidity balance is expressed as:

$$(\ln q)'^{b} = \begin{cases} \left[-\frac{1}{\bar{p}}\right] p' + \left[\Pi \frac{d\ln e_s}{dT}\Big|_{\bar{T}} + \beta_{sat,ocean}\right] \theta' & \text{(Close to saturation, over open ocean)} \\ \left[-\frac{1}{\bar{p}}\right] p' + \left[\Pi \frac{d\ln e_s}{dT}\Big|_{\bar{T}} + \beta_{sat,land}\right] \theta' & \text{(Close to saturation, over land)} \\ \left[-\frac{1}{\bar{p}}\right] p' + \left[\Pi \frac{d\ln e_s}{dT}\Big|_{\bar{T}} + \beta_{sat,ice}\right] \theta' & \text{(Close to saturation, over sea ice)} \\ \left[-\frac{1}{\bar{p}}\right] p' + \left[\beta_{subsat,ocean}\right] \theta' & \text{(Far from saturation, over open ocean)} \\ \left[-\frac{1}{\bar{p}}\right] p' + \left[\beta_{subsat,land}\right] \theta' & \text{(Far from saturation, over land)} \\ \left[-\frac{1}{\bar{p}}\right] p' + \left[\beta_{subsat,ice}\right] \theta' & \text{(Far from saturation, over sea ice)} \end{cases}, \tag{17}$$

where the coefficients multiplying p' and θ' constitute the diagonals of $\mathbf{k}_{q,p}$ and $\mathbf{k}_{q,\theta}$ in Eq. 9, respectively. We find that this relatively simple conditional regression model properly captures the specific humidity balance by assessing this model over the validation period. This is illustrated in Fig. 1c, which shows the grid-point-wise correlation map between θ' and $(\ln q)'^{ub} = (\ln q)' -$

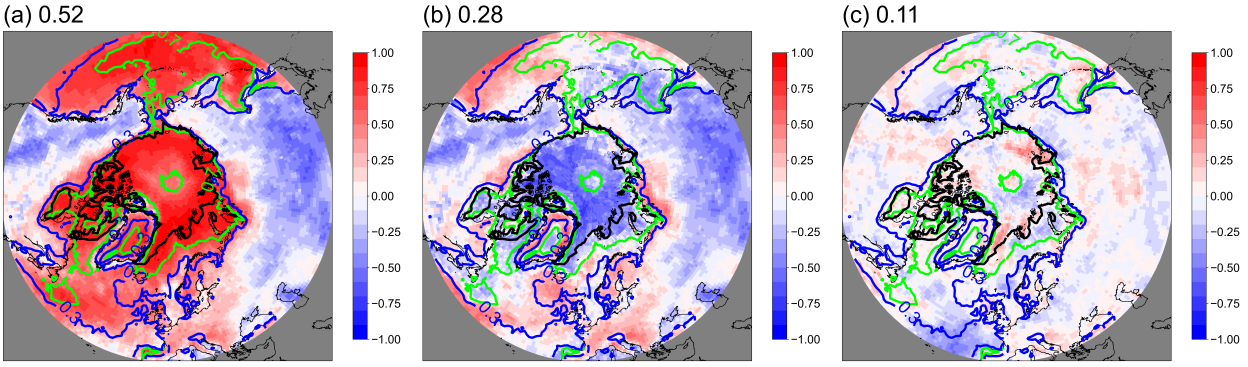

FIG. 1. Geographic distribution of grid-point-wise correlations between potential temperature errors (θ') and (a) specific humidity errors ($(\ln q)'$), (b) specific humidity errors after removing local thermodynamic balance $(\ln q)' - (\ln q)'_{local}$, and (c) unbalanced specific humidity errors ($(\ln q)'_{unb}$). The map is shown for July, 3-6 UTC computed using the validation set that were left out during the covariance training. The blue (0.3) and green (0.7) contours show the fraction of samples that were considered close to saturation within the validation set. The black contour shows the mean sea ice extent (areas with sea ice fraction greater than 0.15) over the validation period. The numerical values on the top left of the plots are mean correlation magnitudes over the domain.

$(\ln q)'^{b}$. The correlations between $(\ln q)'^{ub}$ and θ' are very low, with a domain-average of 0.11, indicating that the dependence of $(\ln q)'$ on θ' has been modeled well enough to be removed.

3) WIND BALANCE

Wind balance is modeled using the linearized Ekman layer equations:

$$u' = -\frac{1}{f}\left(\frac{1}{\bar{\rho}}\frac{\partial p'}{\partial y} + g\frac{\partial z'}{\partial y}\right) - \frac{C_d\left|\bar{\mathbf{V}}\right|}{f\bar{z}}v', \tag{18}$$

$$v' = \frac{1}{f}\left(\frac{1}{\bar{\rho}}\frac{\partial p'}{\partial x} + g\frac{\partial z'}{\partial x}\right) + \frac{C_d\left|\bar{\mathbf{V}}\right|}{f\bar{z}}u', \tag{19}$$

where $\left|\bar{\mathbf{V}}\right| = \sqrt{\bar{u}^2 + \bar{v}^2}$ and C_d is the non-dimensional drag coefficient; see Appendix B for details on the linearization. Equations 18 and 19 can be combined to yield an explicit form for u' and v'

shown by:

$$
\begin{aligned}
u' &= u'_{mass} + u'_{friction} \\
&= K_{u,mass}\left[-\frac{1}{f}\left(\frac{1}{\bar{\rho}}\frac{\partial p'}{\partial y} + g\frac{\partial z'}{\partial y}\right)\right] + K_{u,friction}\left[-\frac{|\bar{\mathbf{V}}|}{f^2\bar{z}}\left(\frac{1}{\bar{\rho}}\frac{\partial p'}{\partial x} + g\frac{\partial z'}{\partial x}\right)\right], \qquad (20)
\end{aligned}
$$

$$
\begin{aligned}
v' &= v'_{mass} + v'_{friction} \\
&= K_{v,mass}\left[\frac{1}{f}\left(\frac{1}{\bar{\rho}}\frac{\partial p'}{\partial x} + g\frac{\partial z'}{\partial x}\right)\right] + K_{v,friction}\left[-\frac{|\bar{\mathbf{V}}|}{f^2\bar{z}}\left(\frac{1}{\bar{\rho}}\frac{\partial p'}{\partial y} + g\frac{\partial z'}{\partial y}\right)\right], \qquad (21)
\end{aligned}
$$

where $K_{u,mass}$ and $K_{v,mass}$ are coefficients that define the strength of mass-wind coupling, and $K_{u,friction}$ and $K_{v,friction}$ are coefficients that define the influence of turbulent friction on wind fields. The four coefficients are obtained by regressing the bracketed forcing terms on the right-hand side of Eqs. 20 and 21 onto the wind perturbations. It is worth noting that the regression coefficients are non-dimensional, and any dependence of the balance on the mean state is incorporated into the forcing terms. The balance operators for u' and v' in Eq. 9 can be expressed using the four regression coefficients as:

$$k_{u,p} = -\frac{K_{u,mass}}{f\bar{\rho}}\frac{\partial}{\partial y} - \frac{K_{u,friction}|\bar{\mathbf{V}}|}{f^2\bar{\rho}\bar{z}}\frac{\partial}{\partial x}, \qquad (22)$$

$$k_{u,z} = -\frac{K_{u,mass}g}{f}\frac{\partial}{\partial y} - \frac{K_{u,friction}|\bar{\mathbf{V}}|g}{f^2\bar{z}}\frac{\partial}{\partial x}, \qquad (23)$$

$$k_{v,p} = \frac{K_{v,mass}}{f\bar{\rho}}\frac{\partial}{\partial x} - \frac{K_{v,friction}|\bar{\mathbf{V}}|}{f^2\bar{\rho}\bar{z}}\frac{\partial}{\partial y}, \qquad (24)$$

$$k_{v,z} = \frac{K_{v,mass}g}{f}\frac{\partial}{\partial x} - \frac{K_{v,friction}|\bar{\mathbf{V}}g|}{f^2\bar{z}}\frac{\partial}{\partial y}, \qquad (25)$$

where $k_{u,p}$, $k_{u,z}$, $k_{v,p}$, and $k_{v,z}$ constitute the diagonals of $\mathbf{k}_{u,p}$, $\mathbf{k}_{u,z}$, $\mathbf{k}_{v,p}$, and $\mathbf{k}_{v,z}$, respectively. The horizontal gradient operators in Eqs. 20 – 25 are approximated using a 2nd-order centered difference scheme.

An example of how wind perturbations are partitioned into balanced and unbalanced components is illustrated in Fig. 2, which shows a map of pressure perturbations (p'; colormaps in Fig. 2)

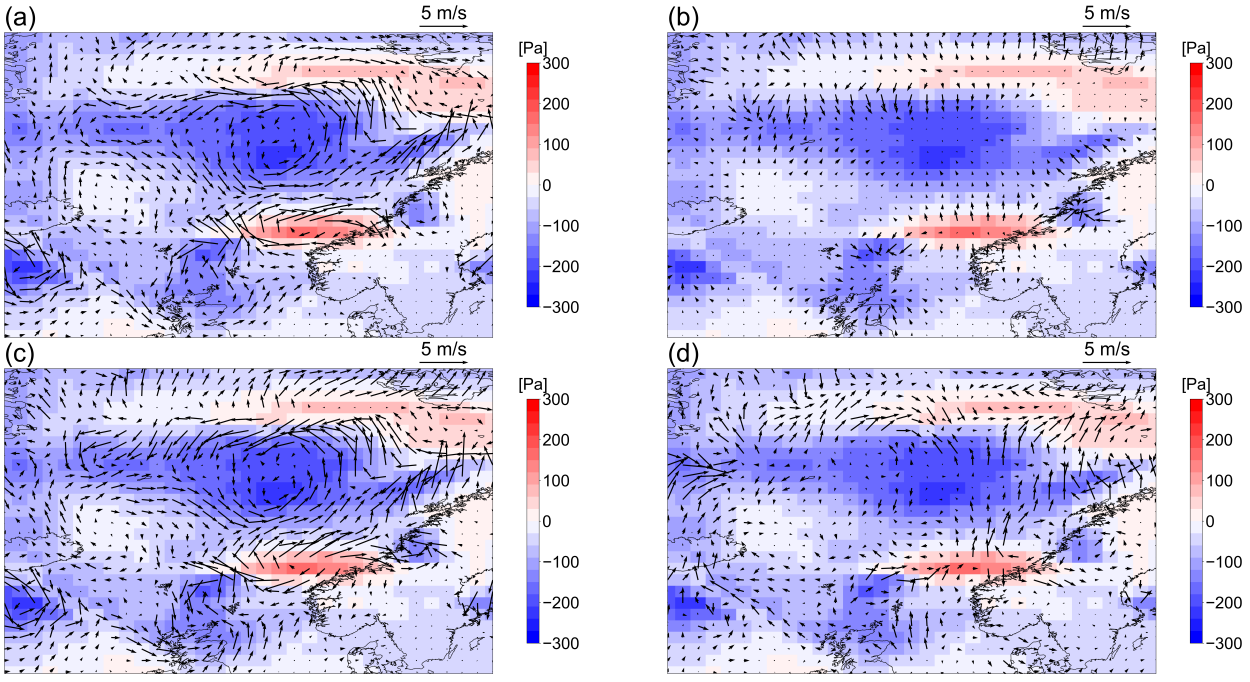

FIG. 2. Map of pressure perturbations (p') and horizontal wind perturbations ($\mathbf{V}' = (u', v')$) shown by the colormaps and vectors, respectively. The wind perturbations are partitioned into (a) component induced by the mass perturbation ($\mathbf{V}'_{mass}$), (b) component induced by turbulent friction ($\mathbf{V}'_{friction}$), (c) balanced wind (i.e., sum of wind induced by the mass perturbation and turbulent friction; $\mathbf{V}'^{b}$), and (d) unbalanced wind ($\mathbf{V}'^{ub}$). The case being shown is a single sample from the validation set obtained on July 1st, 2019 at 6 UTC.

and the corresponding horizontal wind perturbations ($\mathbf{V}' = (u', v')$; vectors in Fig. 2) for a single sample from the validation set. The panels in Fig. 2 show wind perturbations induced by mass perturbation ($\mathbf{V}'_{mass} = (u'_{mass}, v'_{mass})$); Fig. 2a), wind perturbations induced by turbulent friction ($\mathbf{V}'_{friction} = (u'_{friction}, v'_{friction})$); Fig. 2b), balanced wind perturbations ($\mathbf{V}'^{b} = \mathbf{V}'_{mass} + \mathbf{V}'_{friction}$; Fig. 2c), and unbalanced wind perturbations ($\mathbf{V}'^{ub} = \mathbf{V}' - \mathbf{V}'^{b}$; Fig. 2d), respectively. $\mathbf{V}'_{mass}$ show geostrophic-like patterns with cyclonic and anticyclonic wind perturbations corresponding to negative and positive pressure perturbations, respectively (Fig. 2a). $\mathbf{V}'_{friction}$ creates cross-isobaric wind components (Fig. 2b), the magnitudes of which are proportional to the wind speed. Although $\mathbf{V}'_{friction}$ is relatively small in magnitude, its influence on $\mathbf{V}'^{b}$ is visible through cross-isobaric flows present in Fig. 2c. The residual wind perturbations ($\mathbf{V}'^{ub}$), shown in Fig. 2d, are generally uncorrelated with the background mass perturbations and are treated as such in this study.

4) Radiation balance

The radiation field in CAM6 forcings consists of 5 variables which are one broadband longwave flux (F_{lw}) and the direct and diffuse components of shortwave fluxes in the near-infrared and visible channels (F_{nr}, F_{vr}, F_{nf}, and F_{vf}). While most previous forcing perturbation methods have worked with net shortwave flux, the partitioning of shortwave fluxes into 4 components allows for more sophisticated radiative transfer schemes in contemporary ice models, such as the Los Alamos sea ice model (CICE), to be utilized meaningfully (Hunke et al. 2015). Therefore, we retain the 4-component representation of the shortwave fluxes in our error covariance model.

The balance operator for radiation perturbations corresponds to the lower right block of Eq. 9. The diagonals of each sub-matrix are estimated from linear regression that is performed conditionally on the fraction of diffuse shortwave radiation to net shortwave radiation of the mean state shown by:

$$r_{df} = \frac{\bar{F}_{nf} + \bar{F}_{vf}}{\bar{F}_{nr} + \bar{F}_{vr} + \bar{F}_{nf} + \bar{F}_{vf}}. \tag{26}$$

The values of r_{df} have a physical interpretation, in that samples with higher values of r_{df} would correspond to those with an optically thick atmosphere, either due to larger extinction coefficients or a longer optical path (Petty 2006). We find that the relationship between radiation perturbations varies strongly as a function of r_{df}. This is illustrated in Fig. 3, which shows maps of grid-point-wise covariance between F'_{nr} and F'_{nf} that have been stratified according to the values of r_{df}. From the upper left to lower right panel in Fig. 3 are covariances that have been estimated using samples with r_{df}, ranging from [0, 0.1), [0.1, 0.2), ..., [0.8, 0.9), and [0.9, 1]. For $r_{df} < 0.5$, F'_{nr} and F'_{nf} have a negative covariance (top row of Fig. 3). For $r_{df} \geq 0.5$, the negative covariance between F'_{nr} and F'_{nf} begins to weaken to the point at which for $0.9 \leq r_{df} \leq 1$ the dominant covariance becomes positive (lower right panel of Fig. 3). Therefore, linear regression is performed conditionally by stratifying the training dataset into 5 ranges of r_{df} values ([0, 0.5), [0.5, 0.7), [0.7, 0.8), [0.8, 0.9),

[0.9, 1]). For a given r_{df} bin, the formula used for linear regression is given by:

$$\begin{bmatrix} \widetilde{\mathbf{F}'_{lw}} \\ \widetilde{\mathbf{F}'_{nr}} \\ \widetilde{\mathbf{F}'_{vr}} \\ \widetilde{\mathbf{F}'_{nf}} \\ \widetilde{\mathbf{F}'_{vf}} \end{bmatrix} = \begin{bmatrix} \boldsymbol{\sigma}^{\dagger}_{lw}\mathbf{F}'_{lw} \\ \boldsymbol{\sigma}^{\dagger}_{nr}\mathbf{F}'_{nr} \\ \boldsymbol{\sigma}^{\dagger}_{vr}\mathbf{F}'_{vr} \\ \boldsymbol{\sigma}^{\dagger}_{nf}\mathbf{F}'_{nf} \\ \boldsymbol{\sigma}^{\dagger}_{vf}\mathbf{F}'_{vf} \end{bmatrix} = \begin{bmatrix} \mathbf{I} & \mathbf{0} & \mathbf{0} & \mathbf{0} & \mathbf{0} \\ \boldsymbol{\beta}_{nr,lw} & \mathbf{I} & \mathbf{0} & \mathbf{0} & \mathbf{0} \\ \boldsymbol{\beta}_{vr,lw} & \boldsymbol{\beta}_{vr,nr} & \mathbf{I} & \mathbf{0} & \mathbf{0} \\ \boldsymbol{\beta}_{nf,lw} & \boldsymbol{\beta}_{nf,nr} & \boldsymbol{\beta}_{nf,vr} & \mathbf{I} & \mathbf{0} \\ \boldsymbol{\beta}_{vf,lw} & \boldsymbol{\beta}_{vf,nr} & \boldsymbol{\beta}_{vf,vr} & \boldsymbol{\beta}_{vf,vr} & \mathbf{I} \end{bmatrix} \begin{bmatrix} \mathbf{F}'^{ub}_{lw} \\ \mathbf{F}'^{ub}_{nr} \\ \mathbf{F}'^{ub}_{vr} \\ \mathbf{F}'^{ub}_{nf} \\ \mathbf{F}'^{ub}_{vf} \end{bmatrix}. \tag{27}$$

Here, $\boldsymbol{\sigma}$ and $\boldsymbol{\beta}$ are diagonal matrices with grid-point-wise standard deviations of the radiation perturbations and regression coefficients along the diagonals. Notably, the normalization (i.e., $\widetilde{\mathbf{F}'} = \boldsymbol{\sigma}^{\dagger}\mathbf{F}'$) is done prior to computing the regression coefficients, thus the unbalanced components of radiation perturbations are non-dimensional. Similar to that of specific humidity balance, both $\boldsymbol{\sigma}$ and $\boldsymbol{\beta}$ are only estimated when there are more than 80 samples available. If not enough samples occur at a given grid point and r_{df} bin, the average values of σ's and β's collected within ±0.05 of the current cosine solar zenith angle within the current r_{df} bin are used to fill in the missing values. Interpolated values of $\boldsymbol{\sigma}$ and $\boldsymbol{\beta}$ are rarely required when tested over the validation data. Equation 27 can be rewritten in the same form as Eq. 9 as:

$$\begin{aligned} \begin{bmatrix} \mathbf{F}'_{lw} \\ \mathbf{F}'_{nr} \\ \mathbf{F}'_{vr} \\ \mathbf{F}'_{nf} \\ \mathbf{F}'_{vf} \end{bmatrix} &= \begin{bmatrix} \boldsymbol{\sigma}_{lw} & \mathbf{0} & \mathbf{0} & \mathbf{0} & \mathbf{0} \\ \mathbf{0} & \boldsymbol{\sigma}_{nr} & \mathbf{0} & \mathbf{0} & \mathbf{0} \\ \mathbf{0} & \mathbf{0} & \boldsymbol{\sigma}_{vr} & \mathbf{0} & \mathbf{0} \\ \mathbf{0} & \mathbf{0} & \mathbf{0} & \boldsymbol{\sigma}_{nf} & \mathbf{0} \\ \mathbf{0} & \mathbf{0} & \mathbf{0} & \mathbf{0} & \boldsymbol{\sigma}_{vf} \end{bmatrix} \begin{bmatrix} \widetilde{\mathbf{F}'_{lw}} \\ \widetilde{\mathbf{F}'_{nr}} \\ \widetilde{\mathbf{F}'_{vr}} \\ \widetilde{\mathbf{F}'_{nf}} \\ \widetilde{\mathbf{F}'_{vf}} \end{bmatrix} \\ &= \begin{bmatrix} \boldsymbol{\sigma}_{lw} & \mathbf{0} & \mathbf{0} & \mathbf{0} & \mathbf{0} \\ \boldsymbol{\sigma}_{nr}\boldsymbol{\beta}_{nr,lw} & \boldsymbol{\sigma}_{nr} & \mathbf{0} & \mathbf{0} & \mathbf{0} \\ \boldsymbol{\sigma}_{vr}\boldsymbol{\beta}_{vr,lw} & \boldsymbol{\sigma}_{vr}\boldsymbol{\beta}_{vr,nr} & \boldsymbol{\sigma}_{vr} & \mathbf{0} & \mathbf{0} \\ \boldsymbol{\sigma}_{nf}\boldsymbol{\beta}_{nf,lw} & \boldsymbol{\sigma}_{nf}\boldsymbol{\beta}_{nf,nr} & \boldsymbol{\sigma}_{nf}\boldsymbol{\beta}_{nf,vr} & \boldsymbol{\sigma}_{nf} & \mathbf{0} \\ \boldsymbol{\sigma}_{vf}\boldsymbol{\beta}_{vf,lw} & \boldsymbol{\sigma}_{vf}\boldsymbol{\beta}_{vf,nr} & \boldsymbol{\sigma}_{vf}\boldsymbol{\beta}_{vf,vr} & \boldsymbol{\sigma}_{vf}\boldsymbol{\beta}_{vf,vr} & \boldsymbol{\sigma}_{vf} \end{bmatrix} \begin{bmatrix} \mathbf{F}'^{ub}_{lw} \\ \mathbf{F}'^{ub}_{nr} \\ \mathbf{F}'^{ub}_{vr} \\ \mathbf{F}'^{ub}_{nf} \\ \mathbf{F}'^{ub}_{vf} \end{bmatrix}, \end{aligned} \tag{28}$$

where we have multiplied Eq. 27 on both sides by a matrix consisted of $\boldsymbol{\sigma}$s in its diagonal blocks.

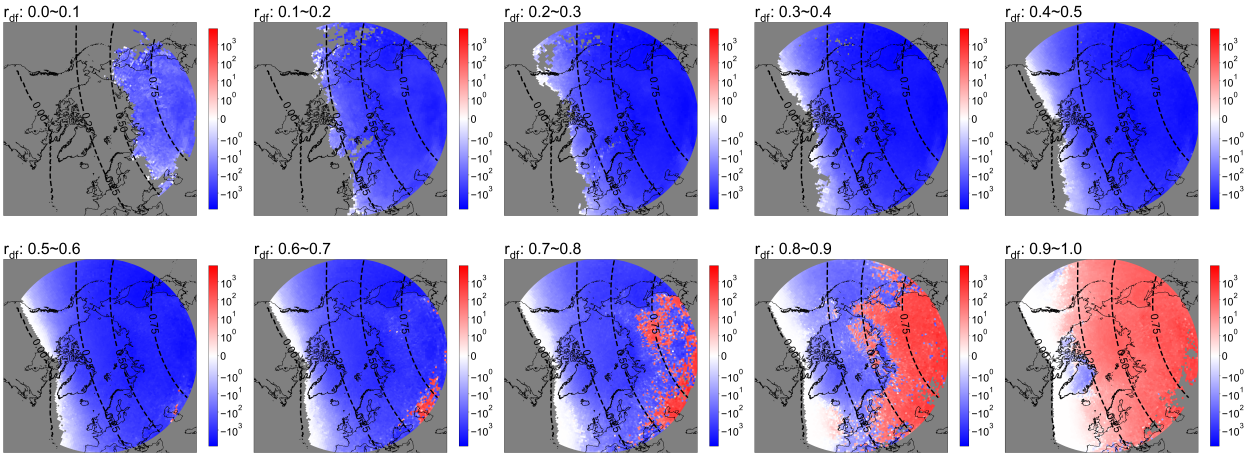

FIG. 3. Map of grid-point-wise covariance between the errors in direct (F'_{nr}) and diffuse (F'_{nf}) components of near-infrared shortwave radiation stratified according to the fraction of diffuse shortwave radiation to net shortwave radiation (r_{df}). From the upper left to the lower right panel are stratified covariances for r_{df} ranged from [0, 0.1), [0.1, 0.2), ..., [0.8, 0.9), [0.9, 1]. The colormaps are shown in base-10 log-scale except for the range in (-1, 1), which is shown in a linear scale. The dotted contours denote the cosine of the solar zenith angle. The covariances shown are computed using the training data subset for July 3-6 UTC.

In this study, radiation perturbations are treated independently of state perturbations (p', θ', q', u', and v'), as shown by the zero matrices in the lower left blocks of Eq. 9. This is done for two reasons: (1) The radiation variables provided in the CAM6 forcing fields are radiative fluxes that are received by the surface and not those absorbed by the lowest model layer. Thus, it is difficult to formulate an analytical argument to identify potential correlations between the two fields. (2) When cross-correlations are computed between the radiation and state perturbations, they remain relatively small (not shown).

c. Spatial operator

$\mathbf{K}$ approximates the block-diagonalization of $\hat{\mathbf{P}}$ as follows:

$$\hat{\mathbf{P}} \approx \mathbf{K}\hat{\mathbf{P}}^{ub}\mathbf{K}^T = \mathbf{K}\begin{bmatrix} \hat{\mathbf{P}}_1^{ub} & \mathbf{0} & \dots & \mathbf{0} \\ \mathbf{0} & \hat{\mathbf{P}}_2^{ub} & \dots & \mathbf{0} \\ \dots & & & \\ \mathbf{0} & \mathbf{0} & \dots & \hat{\mathbf{P}}_{10}^{ub} \end{bmatrix}\mathbf{K}^T. \tag{29}$$

Since $\hat{\mathbf{P}}^{ub}$ is assumed to be block-diagonal, each sub-matrix $\hat{\mathbf{P}}_i^{ub}$ is treated independently. To complete the diagonalization, we perform singular value decomposition to each of the normalized $\hat{\mathbf{P}}_i^{ub}$s shown by:

$$\mathbf{d}_i^{\dagger}\hat{\mathbf{P}}_i^{ub}\mathbf{d}_i^{\dagger} = \mathbf{u}_i\mathbf{s}_i\mathbf{u}_i^T. \tag{30}$$

Here, $\mathbf{d}_i \in \mathbb{R}^{K\times K}$ is a diagonal matrix with the grid-point standard deviation of the unbalanced component on its diagonal, $\mathbf{s}_i \in \mathbb{R}^{S\times S}$ is a diagonal matrix with the largest S singular values on its diagonal, and $\mathbf{u}_i \in \mathbb{R}^{K\times S}$ is a rectangular matrix with the corresponding singular vectors in its columns (Purser et al. 2003a,b). For each $\hat{\mathbf{P}}_i^{ub}$, S is chosen such that the explained variance is at least over 99% for all months and TOD (Fig. 4). The operators $\mathbf{d}_i$, $\mathbf{s}_i$, and $\mathbf{u}_i$ are used to compute the matrix square root of $\hat{\mathbf{P}}_i^{ub}$ as:

$$\mathbf{g}_i = \mathbf{d}_i\mathbf{u}_i\mathbf{s}_i^{\frac{1}{2}}. \tag{31}$$

$\mathbf{g}_i$'s constitute the diagonal blocks of the spatial operator $\mathbf{G}$, which diagonalizes $\hat{\mathbf{P}}^{ub}$ as follows:

$$\hat{\mathbf{P}}^{ub} = \mathbf{G}\mathbf{I}\mathbf{G}^T = \begin{bmatrix} \mathbf{g}_1 & \mathbf{0} & \dots & \mathbf{0} \\ \mathbf{0} & \mathbf{g}_2 & \dots & \mathbf{0} \\ \dots & & & \\ \mathbf{0} & \mathbf{0} & \dots & \mathbf{g}_{10} \end{bmatrix} \begin{bmatrix} \mathbf{g}_1^T & \mathbf{0} & \dots & \mathbf{0} \\ \mathbf{0} & \mathbf{g}_2^T & \dots & \mathbf{0} \\ \dots & & & \\ \mathbf{0} & \mathbf{0} & \dots & \mathbf{g}_{10}^T \end{bmatrix} \tag{32}$$

d. Temporal operator

The modeled atmospheric forcing perturbation can be derived by sequentially applying the operators $\mathbf{G}$ and $\mathbf{K}$ to a sampled univariate perturbation shown by:

$$\hat{\mathbf{e}}_t = \mathbf{K}_t\mathbf{G}_t\mathbf{z}_t, \quad \mathbf{z}_t \sim \mathcal{N}(\mathbf{0}, \mathbf{I}). \tag{33}$$

The subscript t for operators $\mathbf{G}_t$ and $\mathbf{K}_t$ indicates the selection of an error covariance model within the set defined in Eq. 1 that has the month and the TOD corresponding to time t.

Temporal correlations are modeled using a 1^{st}-order Markov chain:

$$\mathbf{z}_{t+1} = \mathbf{M}_{t:t+1}\mathbf{z}_t + \boldsymbol{\eta}_{t+1}, \quad \boldsymbol{\eta}_{t+1} \sim \mathcal{N}(\mathbf{0}, \mathbf{A}_{t+1}). \tag{34}$$

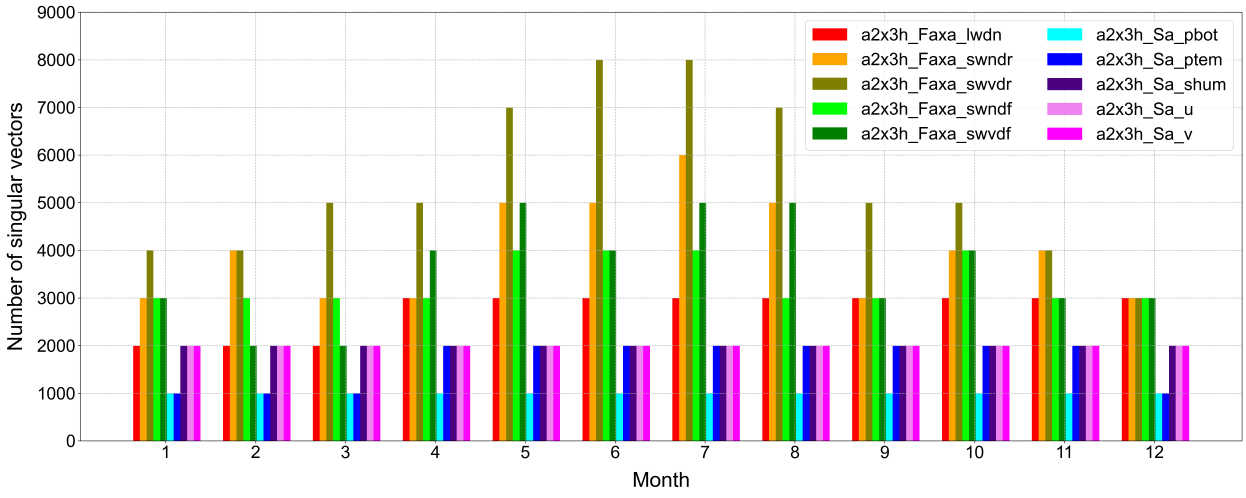

FIG. 4. The number of singular vectors used to represent spatial correlation structure for each variable of the unbalanced component.

Here, the first and second terms on the right-hand side correspond to the time-deterministic and time-stochastic parts, respectively. $\mathbf{M}_{t:t+1}$ is defined by

$$\mathbf{M}_{t:t+1} = \mathbb{E}[\mathbf{z}_{t+1}{\mathbf{z}_t}^T], \tag{35}$$

which is analogous to the one-lag autocorrelation in the scalar case. The expectation in Eq. 35 is estimated from the sample mean of the training data. $\boldsymbol{\eta}_{t+1}$ is a random vector drawn from a zero-mean normal distribution with covariance $\mathbf{A}_{t+1}$. $\mathbf{A}_{t+1}$ is defined as:

$$\begin{aligned} \mathbf{A}_{t+1} &= \mathbb{E}[\boldsymbol{\eta}_{t+1}{\boldsymbol{\eta}_{t+1}}^T], \\ &= \mathbb{E}[(\mathbf{z}_{t+1} - \mathbf{M}_{t:t+1}\mathbf{z}_t)(\mathbf{z}_{t+1} - \mathbf{M}_{t:t+1}\mathbf{z}_t)^T], \\ &= \mathbf{I} - \mathbf{M}_{t:t+1}{\mathbf{M}_{t:t+1}}^T, \end{aligned} \tag{36}$$

which ensures that at any time t, $\mathbf{z}_t$ is a random sample from $\mathcal{N}(\mathbf{0},\mathbf{I})$. In this study, $\mathbf{M}_{t:t+1}$ is assumed block-diagonal shown by:

$$\mathbf{M}_{t:t+1} = \begin{bmatrix} \mathbf{m}_{t:t+1,1} & \mathbf{0} & \dots & \mathbf{0} \\ \mathbf{0} & \mathbf{m}_{t:t+1,2} & \dots & \mathbf{0} \\ \dots & & & \\ \mathbf{0} & \mathbf{0} & \dots & \mathbf{m}_{t:t+1,10} \end{bmatrix}, \tag{37}$$

where $\mathbf{m}_{t:t+1,i}$ denotes the matrix corresponding to the i^{th} variable. This means inter-variable correlations within the unbalanced components are assumed to remain negligible at lag-one, which we find to be a good assumption after examining lag-one cross correlations (not shown). Consequently, according to Eq. 36, $\mathbf{A}_{t+1}$ is also block-diagonal.

e. Using the covariance model

The atmospheric forcing ensemble can be generated by adding perturbations sampled from Eqs. 33 and 34 to any given atmospheric forcing vector as:

$$\hat{\boldsymbol{\psi}}_t^i = \boldsymbol{\psi}_t^* + \mathbf{w}_t \hat{\mathbf{e}}_t^i \quad (i = 1, ..., N_e), \tag{38}$$

where $\hat{\boldsymbol{\psi}}_t$ and $\boldsymbol{\psi}_t^*$ are the perturbed and given atmospheric forcing vectors, respectively. $\mathbf{w}_t$ is a postprocessing mask applied to variables bounded below zero (q, F_{lw}, F_{nr}, F_{vr}, F_{nf}, and F_{vf}) at each model grid shown by:

$$w_t = \begin{cases} 1, & \min\limits_{i=1:N_{ens}} (\psi_t + \hat{e}_t^i) \geq 0 \\ \dfrac{\psi_t}{\psi_t - \min\limits_{i=1:N_{ens}} (\psi_t + \hat{e}_t^i)}, & \min\limits_{i=1:N_{ens}} (\psi_t + \hat{e}_t^i) < 0 \end{cases}. \tag{39}$$

This mask ensures that no negative values occur in the sampled ensemble for such variables.

As mentioned in the introduction, the advantage of a forcing perturbation model is that the distribution can be modified to generate forcing ensembles that contain the desired amount of error variance. This can be achieved with our perturbation model by applying a scale factor, α, to the distribution of $\mathbf{z} \sim \alpha\mathcal{N}(\mathbf{0},\mathbf{I})$. Equation 33 can then be applied to the scaled $\mathbf{z}$ to obtain an inflated

($\alpha > 1$) or deflated ($\alpha < 1$) ensemble that respects the correlation structures encoded in $\mathbf{K}$ and $\mathbf{G}$. We presume that a forcing ensemble sampled from our covariance models with no scaling applied will likely be under-dispersed relative to real-world atmospheric forcing errors. This is because, as mentioned in Section 3a, model errors are not taken into account in the error covariance models. Furthermore, since the training data are time averages, error variances in the covariance models are likely to be underestimated.

4. Sample statistics of the error covariance model

Here, we illustrate key properties of our error covariance models by comparing statistics of perturbations sampled from our error covariance models with statistics of ensemble perturbations from the validation data, namely, atmospheric model states from 2019 and 2020 that were left out during training. The sample statistics are computed from an 80-member ensemble generated from our covariance model centered about the mean state of the reanalysis forcing over the validation period, which we refer to in this section as sample data.

a. Seasonal/Diurnal cycle

Figure 5 shows a map of ensemble standard deviations of F'_{nf} during January (top row of Fig. 5) and July (bottom row of Fig. 5). The ensemble standard deviations are shown over the course of 24 hours at 6-hour intervals starting from 3-6 UTC (left column of Fig. 5) to 21-24 UTC (right column of Fig. 5). The spatial distribution of the magnitude of ensemble standard deviations shows good agreement between the sample (colors in Fig. 5) and validation data (white contours in Fig. 5). Namely, the dependence of the ensemble variance of F'_{nf} on the solar zenith angle (red contours in Fig. 5) is captured well within our covariance models with the magnitudes decaying with larger zenith angles and going to zero where the zenith angle exceeds 90°. More localized features are also captured well by our covariance models with larger ensemble variances from the sample data corresponding to locations where the ensemble variances are high in the validation data. Furthermore, the change in spatial distribution of forcing errors associated with the diurnal (columns of Fig. 5) and seasonal (rows of Fig. 5) cycles is captured in our error covariance models. It is noted that diurnal changes are most significant in variables associated with shortwave forcings,

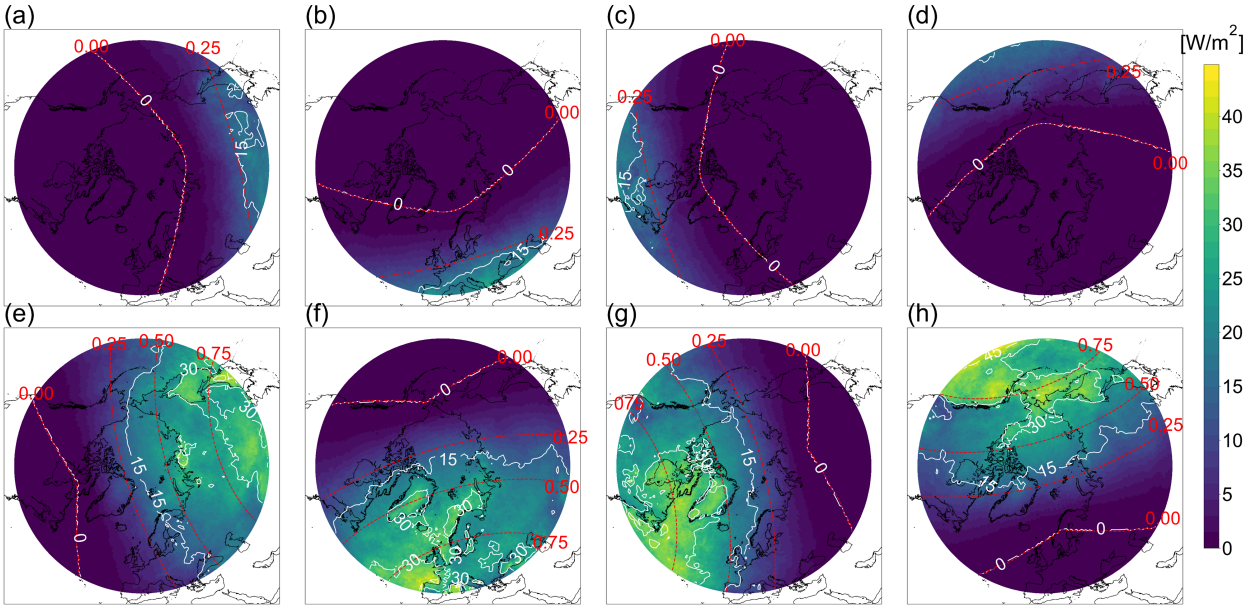

FIG. 5. Geographic distribution of ensemble standard deviation of diffuse near-infrared solar radiation for (top row) January and (bottom row) July over the course of 24 hours. The maps shown represent perturbation magnitudes at (a, e) 3-6 UTC, (b, f) 9-12 UTC, (c, g) 15-18 UTC, and (d, h) 21-24 UTC. The colormap and white contours denote standard deviations computed from the sample and validation data, respectively. The red contours show cosine of the solar zenith angle.

as shown by the distinct spatial patterns in each column of Fig. 5, while seasonal changes are relevant for more variables, including temperature and specific humidity (not shown).

b. Multivariate balance

The modeled specific humidity balance is illustrated in Fig. 6, which shows contours of ensemble estimated correlation coefficients between q' and θ' binned as a function of the mean state T (x-axis in Fig. 6) and e (y-axis in Fig. 6). From left to right, columns of Fig. 6 are contours obtained over the ocean, land, and sea ice during July 2019-2020. The correlation patterns between q' and θ' in the $T-e$ space are similar for the sample (color contours in Fig. 6) and validation data (line contours in Fig. 6) with strong positive correlations corresponding to mean states close to saturation (points close to the blue plots in Fig. 6) and weaker correlations corresponding to mean states far from saturation (points far from the blue plots in Fig. 6). This dependence of correlations on the mean state is very well replicated in the sample data for ocean/ice surfaces (Fig. 6 a and c).

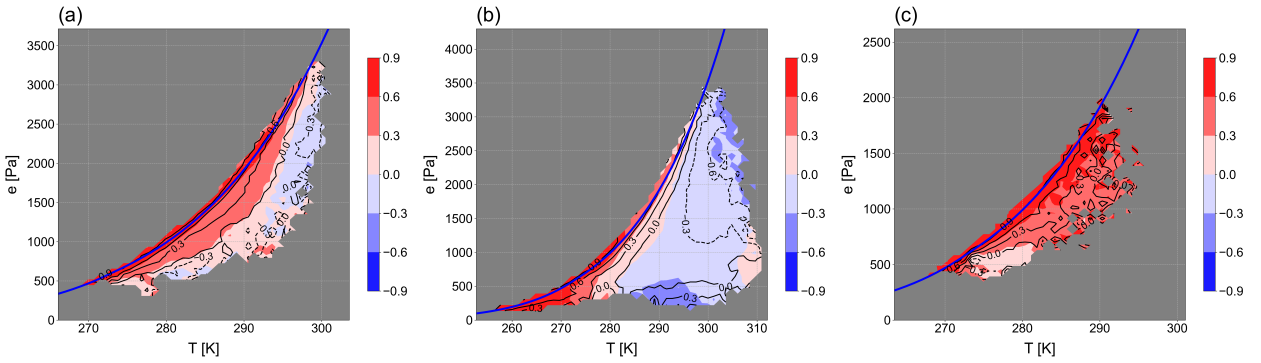

FIG. 6. Contours of ensemble estimated correlation coefficients between specific humidity and potential temperature perturbations binned as a function of the mean state temperature (x-axis) and vapor pressure (y-axis). The colors and lines denote contours from the sample and validation data, respectively. From left to right columns are contours obtained from data over the ocean, land, and sea ice during July 2019-2020 over the Arctic domain (regions north of $40°N$). The thick blue plot is the saturation vapor pressure curve from the Goff-Gratch formula.

Over land surfaces, the correlation patterns from the sample and validation data, although similar, agree less well for points far from the saturation curve (Fig. 6b). This is likely limitations of using a simplistic regression model for non-local specific humidity balance, which we suspect is less ideal for land surfaces that are more heterogeneous and complex relative to the ocean or sea ice. Nevertheless, for the purpose of our perturbation model, which is to use it with a sea ice model, the performance of the balance operator over land surfaces is expected to have a negligible influence on the sea ice model forecasts.

An example of the modeled wind balance is illustrated in Fig. 7a, which shows the map of p' (colormap in Fig. 7a) and the associated wind perturbations from the sample ($\mathbf{V}'^b$; red vectors in Fig. 7a) and validation data ($\mathbf{V}'$; black vectors in Fig. 7a) for a single ensemble member on July 1st, 2019. In general, there is strong agreement with $\mathbf{V}'$ and $\mathbf{V}'^{\mathbf{b}}$ with both wind perturbations following geostrophic-like patterns. Cross-isobaric components of $\mathbf{V}'$ caused by the influence of turbulent friction are also present in $\mathbf{V}'^b$, showing the effects of modeled turbulent friction in the balance operator. To demonstrate more robustly the level of agreement between $\mathbf{V}'$ and $\mathbf{V}'^b$, we compute the component-wise correlations between $\mathbf{V}'$ and $\mathbf{V}'^b$ at each model grid-point using all 80-members over the period of July 2019-2020 (Fig. 7b and c). Overall, the correlations remain

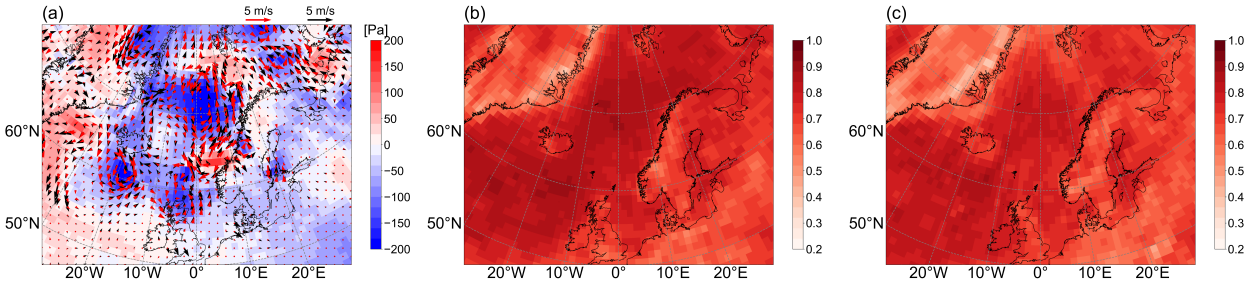

FIG. 7. (a) Map of pressure perturbations (p') and corresponding wind perturbations from a single ensemble member on July 1st, 2019. The black vectors are wind perturbations from the validation data ($\mathbf{V}'$). The red vectors show wind perturbations induced by the underlying mass perturbations as computed by the balance operator ($\mathbf{V}'^{\mathbf{b}}$). Map of grid-point correlations between $\mathbf{V}'$ and $\mathbf{V}'^{\mathbf{b}}$ for the (b) zonal and (b) meridional components. The correlations are evaluated over the period of July 2019-2020.

high with most locations having a correlation above 0.6. Correlations decline in locations with steep topography, which is likely caused by more complex boundary layer processes that are not well explained by the simple bulk parameterization of turbulent friction in our balance operator. Nevertheless, over the ocean/ice surface, correlations between $\mathbf{V}'$ and $\mathbf{V}'^{b}$ are close to 0.9. The good agreement between wind perturbations computed from a full atmospheric model ($\mathbf{V}'$) and wind perturbations estimated by our balance operator ($\mathbf{V}'^{b}$) indicates that our balance operator is capable of inducing wind perturbations that are realistically correlated with the mass field while accounting for the effects of turbulent friction.

The modeled radiation balance is illustrated through an example of the relationship between F'_{nr} and F'_{nf}. This is shown in Fig. 8, which are two dimensional histograms between F'_{nr} (x-axis) and F'_{nf} (y-axis) obtained over the period of July 2019-2020. As mentioned in Section 3b4, the relationship between F'_{nr} and F'_{nf} vary strongly as a function of r_{df}, with predominant negative correlation for $r_{df} < 0.8$ and a shift to a more positive correlation for $r_{df} \geq 0.8$. Both the sample (color contours in Fig. 8) and validation data (line contours in Fig. 8) follow this dependence on r_{df} values as shown by the changing distribution from left to right columns of Fig. 8. However, as seen from the line contours in Fig. 8, the joint distribution of F'_{nr} and F'_{nf} in the validation data appears far from a multivariate Gaussian, particularly for bins with $0.5 \leq r_{df} \leq 0.9$. In such bins, the distribution looks closer to a mixture of two Gaussians—one with a positive and the other with

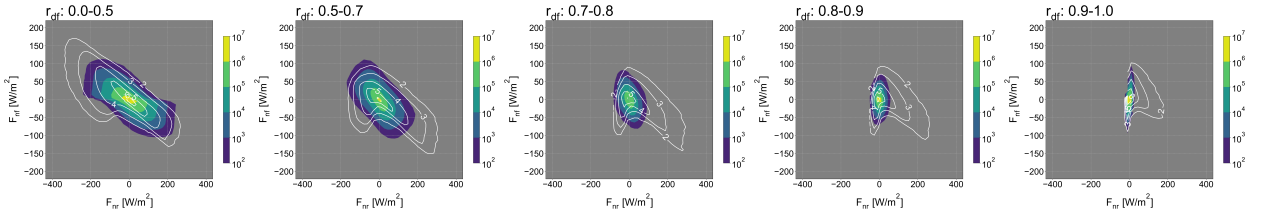

FIG. 8. Two-dimensional histograms between direct near-infrared (x-axis) and diffuse near-infrared (y-axis) solar radiation perturbations showing the number density of data points over the period of July 2019-2020. From left to right panels are histograms that have been stratified according to the percentage of diffuse to net solar radiation of the mean state (r_{df}). The colormaps and contours denote the sample and validation data, respectively.

a negative correlation. This is caused by cases where the ensemble has a range of r_{df} values that are highly non-Gaussian. For example, a sample with half of its ensemble members with $r_{df} = 0.1$ and the other half with $r_{df} = 0.9$ will have a mean $r_{df} = 0.5$, which can occur for situations where over a given grid point, half of the ensembles have clouds while the other half does not. Because we choose to model the radiation balance solely as a function of the ensemble mean r_{df}, such mixed-pixel effects are not allowed to occur in the sample data as seen from the color contours in Fig. 8. Despite the inability of our covariance model to replicate such non-Gaussian distributions, it is still capable of backing out the dominant modes of state-dependent uncertainty in the radiation perturbations.

c. Spatiotemporal covariance

The action of operators **G** and **M**, is illustrated in Fig. 9, which shows a map of spatial correlations centered about (180°, 75°N) for perturbations in downward longwave heat flux (F'_{lw}; Fig. 9a, b, c), zonal wind (u'; Fig. 9d, e, f), and pressure (p'; Fig. 9g, h, i). The correlations are evaluated at time lags of 0 h (left column of Fig. 9), 6 h (middle column of Fig. 9), and 12 h (right column of Fig. 9), for comparison. At a time lag of 0 h (left columns of Fig. 9), the spatial structures of error correlation observed from the sampled data (colormaps in Fig. 9) closely resemble those from the validation data (contours in Fig. 9) for a variety of variables ranging from those with short (Fig. 9a), moderate (Fig. 9d), and long (right column of Fig. 9g) correlation length scales. This demonstrates that the operator **G** effectively models the spatial error correlation structures present

in real-world atmospheric DA systems (in this case, CAM6 DA system). At non-zero time lags of 6 h (middle column of Fig. 9) and 12 h (right column of Fig. 9), weakening correlation magnitudes are observed from both the sampled and validation data. In addition, for pressure (bottom row of Fig. 9), changes in the spatial pattern of error correlation with increasing time lags seen in the validation data are also observed in samples from our error covariance model. This shows that the operator $\mathbf{M}$ in conjunction with $\mathbf{G}$ can propagate the statistics of errors through time in a manner consistent with real-world atmospheric DA systems.

5. Application to a forced sea ice ensemble forecast system

We illustrate the application of our covariance model for generating an ensemble of sea ice model forecasts by performing a set of perfect model experiments. The experiments aim to evaluate two aspects of our covariance model in the context of sea ice forecasting: The ability of the covariance model (1) to replace an ensemble of reanalysis forcings, and (2) to introduce controllable amounts of atmospheric forcing error in the sea ice forecasts through the use of the scale factor discussed in Section 3e while accurately quantifying this error in the ensemble statistics. The experiments are run using version 5.1.2 of CICE (CICE5) within the CESM2 coupling framework (Danabasoglu et al. 2020). CICE5 is a state-of-the-art sea ice model that simulates the evolution of the sea ice thickness distribution and the overlying snow by solving a set of governing equations for dynamical and thermodynamical processes (Hunke et al. 2015). The nature run (i.e., the reference model simulation to be considered as the "truth") for the perfect model experiments is generated by assuming that a single member from the 80-member CAM6/DART atmospheric reanalysis is the true atmospheric forcing. The ocean forcings for all experiments are provided via a slab ocean model (SOM), which approximates the well-mixed ocean layer and provides bottom boundary forcings for the ice model. In this study, the ocean-related parameters that are provided to SOM are the same for all ensemble members and thus do not contribute to the ensemble generation process.

We perform a total of three experiments, each using a different atmospheric forcing ensemble. The first experiment (hereafter EXP1) uses the 80-member reanalysis ensemble and acts as the benchmark for all other experiments. The second experiment (hereafter EXP2) uses an 80-member atmospheric forcing ensemble that is sampled from our covariance model. The forcing ensemble for EXP2 is generated according to the following process: The atmospheric forcing ensemble is first

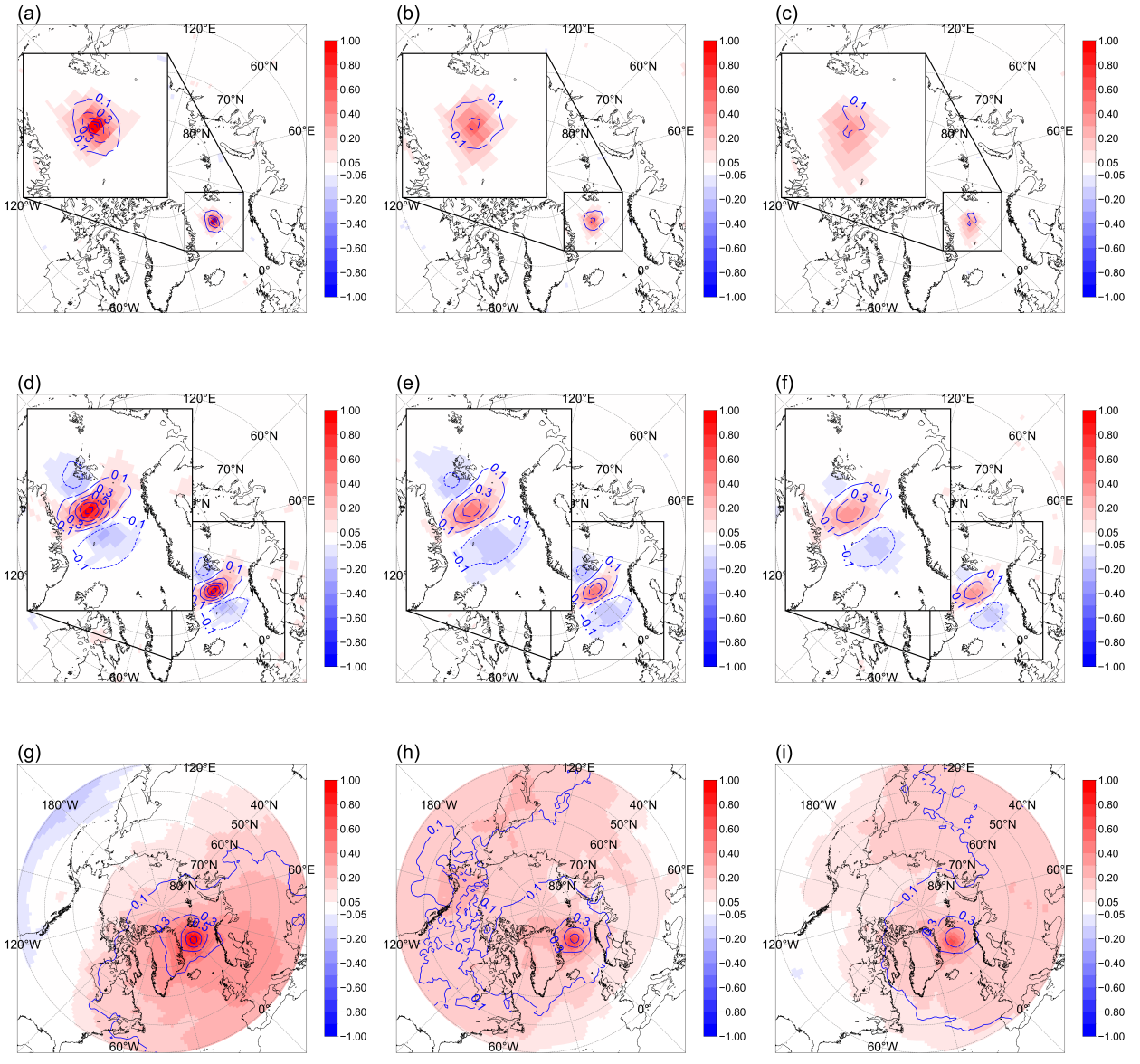

562 FIG. 9. Map of spatial correlation structures centered about (180°, 75°N) for perturbations in (a, b, c)
563 downward longwave heat flux, (d, e, f) zonal wind, and (g, h, i) pressure. The columns show the change in spatial
564 correlation structures with respect to time lags of (left columns) 0h, (middle column) 6h, and (right column) 12h.
565 The colormap and contours show correlations computed from the sampled and validation data, respectively.

588 created by perturbing about the nature run's atmospheric forcing, thus the mean of this ensemble
589 initially corresponds to the true forcing. Then a single member of this ensemble is randomly
590 chosen to be the new ensemble mean and perturbations are added to this new mean, which

now contains non-zero error in the ensemble mean (i.e., forcing error). This two-step process results in an atmospheric forcing ensemble with forcing error and ensemble perturbations that are sampled from the same zero-mean Gaussian distribution, with covariance determined by our error covariance model. The third experiment (hereafter EXP3) also uses a sampled atmospheric forcing ensemble, but the forcing error and ensemble perturbations are sampled from a distribution that has been inflated to twice the original standard deviation. All experiments are re-initialized from the nature run at the beginning of each month to better isolate the influences of the forcing errors from accumulated initial condition errors and potential feedback processes. The experiments are carried out for a single year, starting from March 1st, 2019, which corresponds to part of the validation period set aside during the covariance training.

As verification metrics, we use the root mean squared error (RMSE) and the ensemble standard deviation (SD), which are computed as:

$$\mathrm{RMSE} = \sqrt{\frac{1}{N}\sum_{i=1}^{N}\left(\bar{x}_i - x_i^t\right)}, \tag{40}$$

and

$$\mathrm{SD} = \sqrt{\frac{1}{N}\sum_{i=1}^{N}\left[\frac{1}{N_{ens}-1}\sum_{j=1}^{N_{ens}}\left(x_i^j - \bar{x}_i\right)^2\right]}, \tag{41}$$

where $\bar{x}$ and x^t are the ensemble mean and the nature run, respectively. N is the dimension of the state vector, and N_{ens} is the number of ensemble members. The RMSE and SD each correspond to the actual and the ensemble estimate of error, thus an ensemble with a perfect spread-skill score should have RMSE and SD that are equal.

Figure 10 shows the daily averaged RMSE (solid lines in Fig. 10) and SD (dashed lines in Fig. 10) over the Arctic for sea ice concentration (SIC; Fig. 10a), sea ice thickness (SIT; Fig. 10b), and snow depth (SND; Fig. 10c) for EXP1 (black plots in Fig. 10) and EXP2 (red plots in Fig. 10). In terms of spread-skill score, both EXP1 and EXP2 show good agreement between RMSE and SD. Notably, the spread-skill score shows that the ensemble is well-calibrated the first few days after initialization, but deteriorates with longer forecast lead times. The initially satisfactory spread-skill score is not surprising, given that by design the forcing errors and ensemble perturbations in EXP1 and EXP2 came from the same distribution. Further evidence is provided by spatial distributions of

marginal statistics, illustrated in Figs. 11 and 12, which show maps of 3-day average RMSE (first row of Figs. 11 and 12) and SD (second row of Figs. 11 and 12) for EXP1 (left column of Figs. 11 and 12), EXP2 (middle column of Figs. 11 and 12), and EXP3 (right column of Figs. 11 and 12) for SND forecasts initialized on March 1st, 2019 and September 1st, 2019, respectively. For the individual experiments, the patterns of RMSE appear as random draws from the distribution characterized by SD, which complies with the results shown in Fig. 10. Similar conclusions can be drawn for SIC and SIT; see figures in the appendix.

When examining how well EXP2 replicates atmospheric forcing uncertainty depicted by EXP1, we find that it provides an accurate representation of seasonally varying uncertainty with faster (slower) growing RMSE and SD for forecasts initialized during the Arctic summer (winter) for SIC and SIT. For SND, however, EXP2 tends to produce smaller RMSE/SD during the polar nights (Fig. 10c). This can also be seen in the spatial distribution of RMSE/SD, where EXP2 (middle column of Fig. 11) has smaller magnitudes of RMSE/SD relative to EXP1 (left column of Fig. 11) within the central Arctic. The difference is likely due to the missing precipitation variability within EXP2 since our covariance model does not perturb precipitation. The missing precipitation perturbation appears more impactful during the Arctic winter due to the polar night, whereas during the Arctic summer, the impacts are barely noticeable in the snow forecasts due to the shortwave perturbations manifesting over the entire Arctic basin. This is a limitation in our covariance model that we acknowledge and hope to explore in future work. Fortunately, the seasonal timing at which this limitation is most influential corresponds to the timing at which the SND error growths are small. Thus, the magnitude of the disagreement in RMSE/SD between EXP1 and EXP2 remains small. It is noted that EXP2 is able to replicate the behavior of EXP1 very well during the melting season, where RMSE/SD growth is largest for SND.

EXP3 demonstrates a desirable feature of the covariance model in that it can be used to adjust the sea ice ensemble by controlling the amount of forcing errors/ensemble perturbations that are introduced to the sea ice forecasts. This is illustrated in Fig. 13, which is the same plot as Fig. 10 but shows results from EXP2 (red plots in Fig. 13) and EXP3 (blue plots in Fig. 13). In EXP3, both RMSE/SD become about twice as large as those of EXP2, as intended by the design of the atmospheric forcing ensemble. Like EXP2, the spread-skill score in EXP3 deteriorates with longer forecast lead times. This indicates that the spread-skill relation in the atmospheric forcing

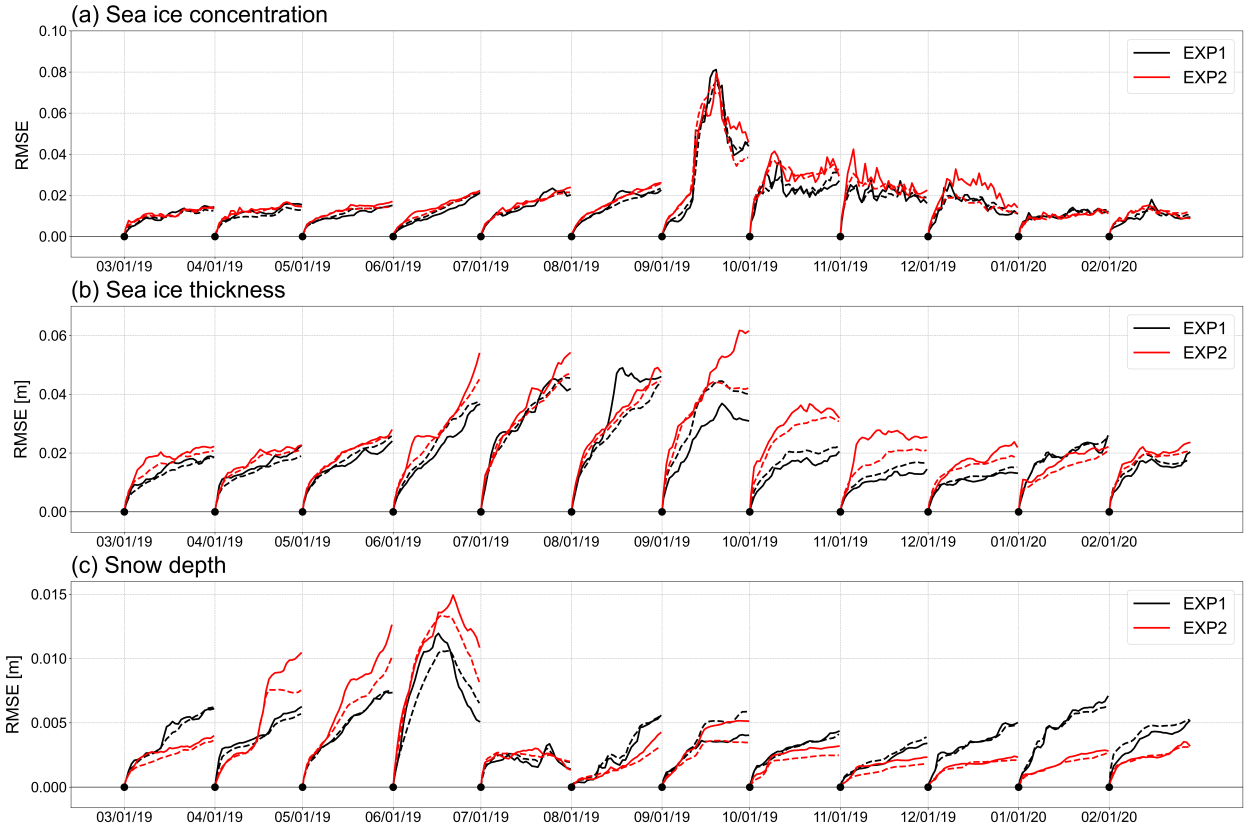

FIG. 10. Timeseries of daily averaged root mean squared error (solid lines) and ensemble spread (dashed lines) for Arctic (a) sea ice concentration, (b) sea ice thickness, and (c) snow depth. The forecasts are initialized from the nature run at the beginning of each month as indicated by the black dots. The black lines denote ensemble forecasts generated from the 80-member reanalysis (EXP1). The red (EXP2) lines denote ensemble forecasts generated using atmospheric forcing ensemble sampled from the perturbation model with a scale factor of 1. The statistics shown are averaged values over grid-cells where the nature run's sea ice concentration is over 0.15.

ensemble maps to those of the sea ice ensemble approximately linearly for shorter-range forecasts, where, for longer forecasts, non-linear effects such as accumulated initial condition errors and feedback processes become more influential. Another point worth noting is that by inflating the atmospheric forcing error/ensemble, the impacts of missing precipitation variability on the SND forecasts in EXP2 (middle column of Fig. 11) are compensated for in EXP3 (right column of Fig. 11). This leads to EXP3 agreeing better with EXP1 in terms of the magnitudes of RMSE/SD for SND forecasts during the Arctic winter relative to EXP2. The ability to adjust the sea ice ensemble in a predictable way has multiple benefits. For instance, in the design of an OSSE, which is an

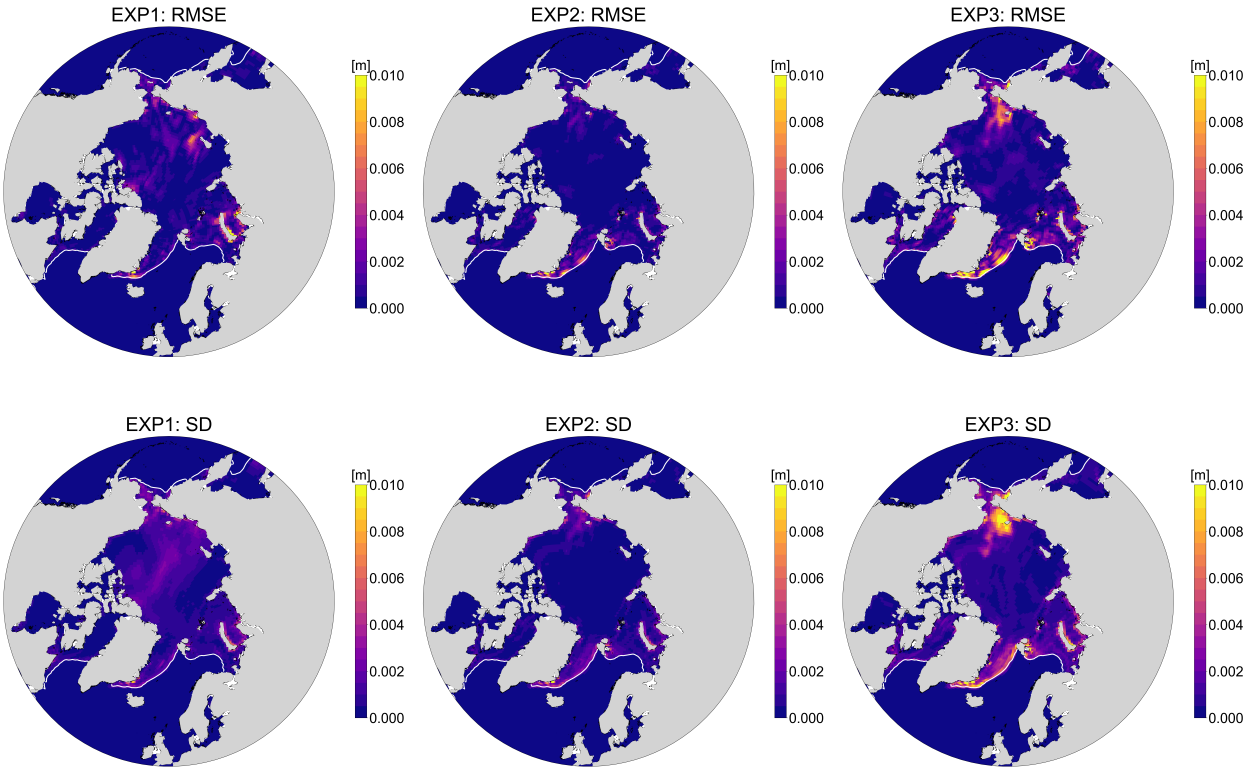

FIG. 11. Maps of (first row) root mean squared error and (second row) ensemble spread of Arctic snow depth averaged over the first 3 days of the forecast initialized on March 1st, 2019. From left to right columns show statistics computed from ensemble forecasts generated from the 80-member reanalysis (EXP1), ensemble forecasts generated using atmospheric forcing ensemble sampled from the perturbation model with a scale factor of 1 (EXP2), and ensemble forecasts generated using atmospheric forcing ensemble sampled from the perturbation model with a scale factor of 2 (EXP3). The white contours shows the 3-day mean mean sea ice extent (areas with sea ice concentration greater than 0.15).

application of the perfect model framework intended to assess the influence of observations on the DA systems. For this purpose, both the error and spread of the ensemble can be tuned to resemble those observed from real-world modeling systems. In real-world applications, where the truth (i.e., nature run) is never known, and thus the error also never known, having means to tune the ensemble spread on the-fly offers much more flexibility on the representation of the background error. As demonstrated in EXP3, the forcing ensemble can be modified to account for sources of background error that were originally omitted, which can be useful for situations where the unaccounted-for sources of background error are difficult to represent in an ensemble forecast, such as model error.

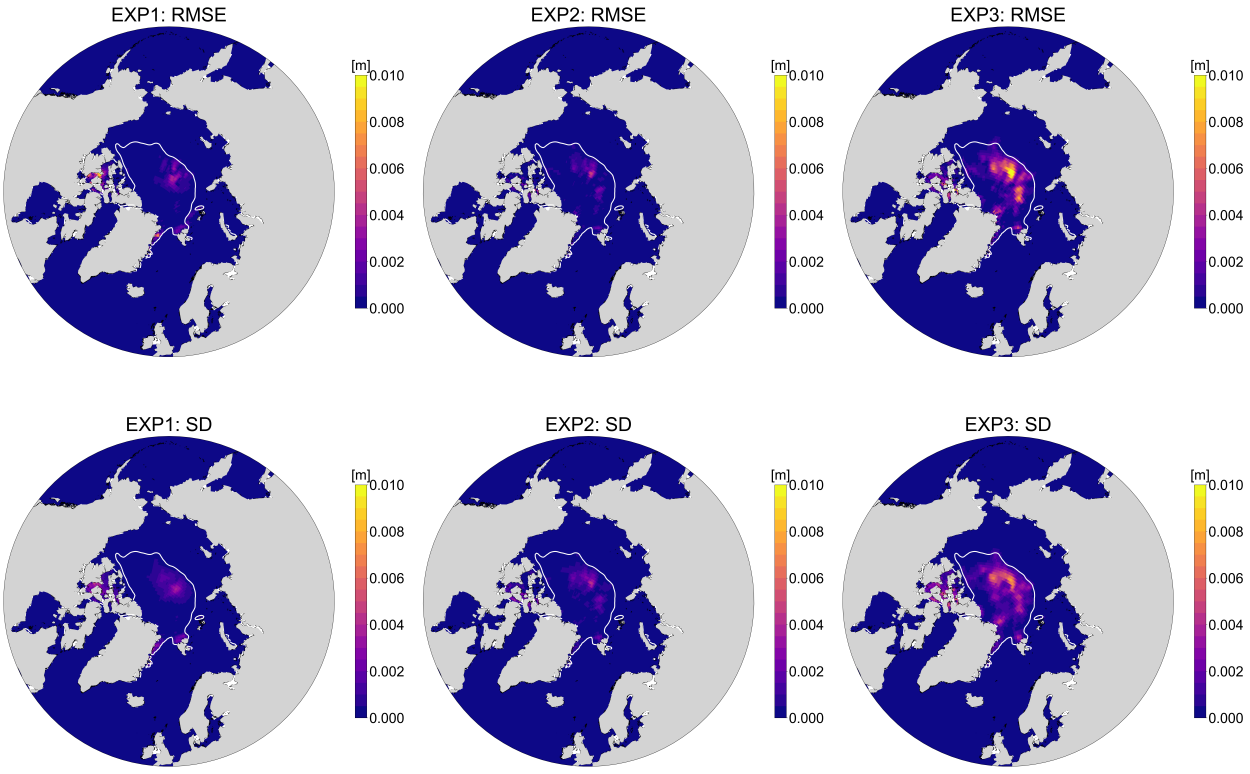

FIG. 12. As in Fig. 11 but for forecasts initialized on September 1st, 2019.

6. Conclusion

This paper introduces an error covariance model for the purpose of simulating realistic error growth in short-term atmospheric forcings over Arctic sea ice relevant to operational sea ice data assimilation experiments. The model generates perturbations that simulate random atmospheric forcing errors associated with short-range (6-h) forecasts. The model accounts for seasonal and diurnal changes in uncertainty, trained from 10 years of 6-h ensemble statistics. Operators that approximate the diagonalization of the error covariances are developed for efficient perturbation sampling. The sample statistics of the error covariance model show good agreement with those of ensemble perturbations from an 80-member atmospheric reanalysis, properly capturing the seasonal/diurnal dependence, the state-dependent multivariate balance, and the spatiotemporal correlation structures.

A set of perfect model experiments using CICE5 demonstrates that our error covariance model is capable of representing the influence of atmospheric forcing errors on short-range sea ice forecasts. In particular, seasonally-varying atmospheric influences on sea ice forecast errors are

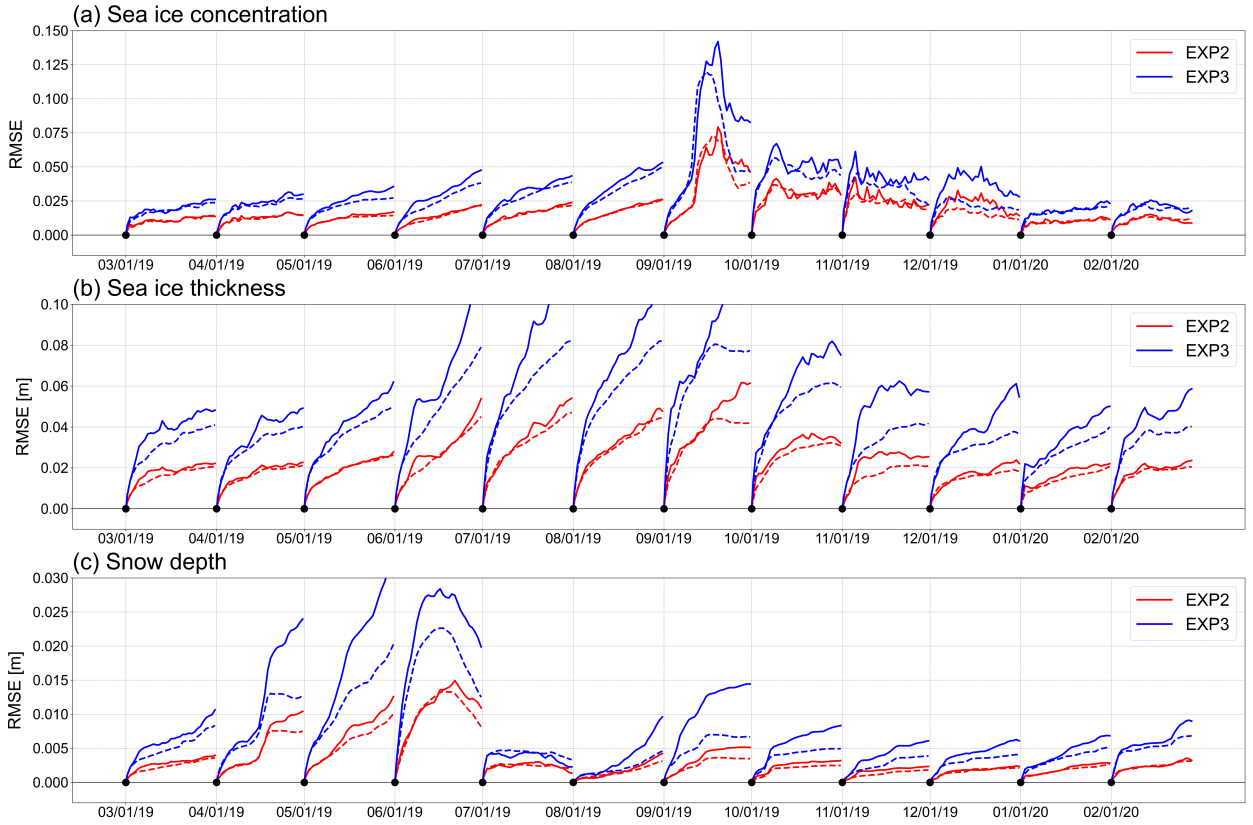

FIG. 13. As in Fig. 10 but for EXP2 (red lines) and EXP3 (blue lines).

well simulated in experiments using our covariance model with faster (slower) growing errors for forecasts initialized during the Arctic summer (winter). At the same time, the sea ice ensembles in the perfect model experiments are shown to provide good estimates of the time-varying sea ice forecast errors. The error covariance model is also capable of controlling for the magnitudes of error and ensemble spread in sea ice forecasts, allowing for generation of sea ice prediction systems with a desired amount of error while preserving good spread-skill score. This flexibility in error/ensemble spread can be beneficial for calibrating both real-world and perfect model sea ice DA systems.

Limitations exist in that the error covariance model is not capable of simulating mixed-pixel effects for radiation perturbation (e.g., cases where ensemble members do not agree on the presence of cloud within a model grid). The model also does not perturb precipitation, which, although relatively minor, has downstream impacts on the Arctic winter snow depth forecasts. Future work will focus on applying this new atmospheric error covariance model to spin up a stand-alone

sea ice OSSE system for exploring the benefits of observations on constraining short-term sea ice/atmosphere forecasts.

Acknowledgments. This work was supported by NOAA grant NA19NES4320002 (Cooperative Institute for Satellite Earth System Studies – CISESS) at the University of Maryland/ESSIC.

Data availability statement. The 80-member CAM6-DART reanalysis are available through https://doi.org/10.5065/JG1E-8525 (Data Assimilation Research Section Computational & Information Systems National Center for Atmospheric Research University Corporation for Atmospheric Research 2020; Raeder et al. 2021). The CESM model codes are available through https://github.com/ESCOMP/CESM/archive/refs/tags/release-cesm2.1.5.zip (Danabasoglu et al. 2020). Python codes used to compute matrix operators of the error covariance model and to sample from the operators are available through https://doi.org/10.5281/zenodo.21014570 (Jung 2026).

APPENDIX A

Variables in the atmospheric forcing state vector

TABLE A1. Name and description of the variables in the atmospheric forcing state vector corresponding to each index.

Index	Sign	Name	Description
1	p	pbot	Pressure at lowest model level
2	θ	ptem	Potential temperature at lowest model level
3	q	shum	Specific humidity at lowest model level
4	u	u	Zonal wind at lowest model level
5	v	v	Meridional wind at lowest model level
6	F_{lw}	lwdn	Downward longwave heat flux
7	F_{nr}	swndr	Direct near-infrared incident solar radiation
8	F_{vr}	swvdr	Direct visible incident solar radiation
9	F_{nf}	swndf	Diffuse near-infrared incident solar radiation
10	F_{vf}	swvdf	Diffuse visible incident solar radiation
11	T	tbot	Temperature at lowest model level
12	z	z	Height at lowest model level as measured from surface topography
13	ρ	dens	Density at lowest model level

APPENDIX B

Derivation of the analytical linearization

a. Model level height

Starting from the hydrostatic equation:

$$\frac{\partial p}{\partial z} = -\frac{pg}{RT} \tag{B1}$$

$$= -\frac{pg}{R_d\left(1+\frac{1-\epsilon}{\epsilon}q\right)\Pi\theta}. \tag{B2}$$

$$\tag{B3}$$

Integrating both sides from the surface to the lowest model level:

$$\int_{z_{sfc}}^{z_{\sigma_0}} dz = -\int_{p_{sfc}}^{p} \frac{R_d\left(1+\frac{1-\epsilon}{\epsilon}q\right)\Pi\theta}{g} d\ln p \tag{B4}$$

$$z_{\sigma_0} - z_{sfc} \approx -\frac{R_d\left(1+\frac{1-\epsilon}{\epsilon}q\right)\Pi\theta}{g}\int_{p_{sfc}}^{p} d\ln p \tag{B5}$$

$$z \approx -\frac{R_d\left(1+\frac{1-\epsilon}{\epsilon}q\right)\Pi\theta}{g}\ln\sigma_0 \tag{B6}$$

, where, $z = z_{\sigma_0} - z_{sfc}$ by definition, $\sigma_0 = \frac{p}{p_{sfc}}$ is a constant, and the approximation denotes assuming constant profiles of q and θ over the integration. This equation can be linearized about a small perturbation about the mean state to give Eq. 12, which is shown by:

$$z' = \frac{\partial z}{\partial\theta}\Big|_{\bar{q}}\theta' + \frac{\partial z}{\partial q}\Big|_{\bar{\theta}}q'. \tag{B7}$$

b. Wind balance

The horizontal momentum equations under a balanced state can be written as:

$$-fv = -\frac{1}{\rho}\frac{\partial p}{\partial x} - g\frac{\partial z}{\partial x} - \frac{C_d|\mathbf{V}|}{z}u, \tag{B8}$$

$$fu = -\frac{1}{\rho}\frac{\partial p}{\partial y} - g\frac{\partial z}{\partial y} - \frac{C_d|\mathbf{V}|}{z}v, \tag{B9}$$

where we have used the bulk approximation to parameterize the effects of turbulent friction (Stull 1988). Equation B8 is linearized with respect to small perturbation about the mean state according to:

$$-f(\bar{v}+v') \approx -\frac{1}{\bar{\rho}+\rho'}\frac{\partial(\bar{p}+p')}{\partial x} - g\frac{\partial(\bar{z}+z')}{\partial x} - \frac{C_d\left|\bar{\mathbf{V}}\right|}{\bar{z}}(\bar{u}+u') \tag{B10}$$

$$\approx -\frac{1}{\bar{\rho}}\left(1-\frac{\rho'}{\bar{\rho}}\right)\frac{\partial(\bar{p}+p')}{\partial x} - g\frac{\partial(\bar{z}+z')}{\partial x} - \frac{C_d\left|\bar{\mathbf{V}}\right|}{\bar{z}}(\bar{u}+u') \tag{B11}$$

$$= \left[-\frac{1}{\bar{\rho}}\frac{\partial\bar{p}}{\partial x} - g\frac{\partial\bar{z}}{\partial x} - \frac{C_d\left|\bar{\mathbf{V}}\right|}{\bar{z}}\bar{u}\right] + \left[-\frac{1}{\bar{\rho}}\frac{\partial p'}{\partial x} - g\frac{\partial z'}{\partial x} - \frac{C_d\left|\bar{\mathbf{V}}\right|}{\bar{z}}u'\right] + \left[-\frac{\rho'}{\bar{\rho}^2}\frac{\partial(\bar{p}+p')}{\partial x}\right]. \tag{B12}$$

Here, the approximation in Eq. B10 denotes $\frac{C_d|\mathbf{V}|}{z} \approx \frac{C_d|\bar{\mathbf{V}}|}{\bar{z}}$, and the approximation in Eq. B11 is $\frac{1}{\bar{\rho}+\rho'} \approx \frac{1}{\bar{\rho}}\left(1-\frac{\rho'}{\bar{\rho}}\right)$. The first term in Eq. B12 cancels with $-f\bar{v}$ on the left-hand side and the last term in Eq. B12 is found to be small relative to the other terms. Therefore, Eq. B12 simplifies to:

$$-fv' \approx -\frac{1}{\bar{\rho}}\frac{\partial p'}{\partial x} - g\frac{\partial z'}{\partial x} - \frac{C_d\left|\bar{\mathbf{V}}\right|}{\bar{z}}u'. \tag{B13}$$

Equation. B9 is linearized following a similar process, which gives:

$$fu' \approx -\frac{1}{\bar{\rho}}\frac{\partial p'}{\partial y} - g\frac{\partial z'}{\partial y} - \frac{C_d\left|\bar{\mathbf{V}}\right|}{\bar{z}}v'. \tag{B14}$$

APPENDIX C

Maps of Spread-Skill for sea ice concentration and thickness

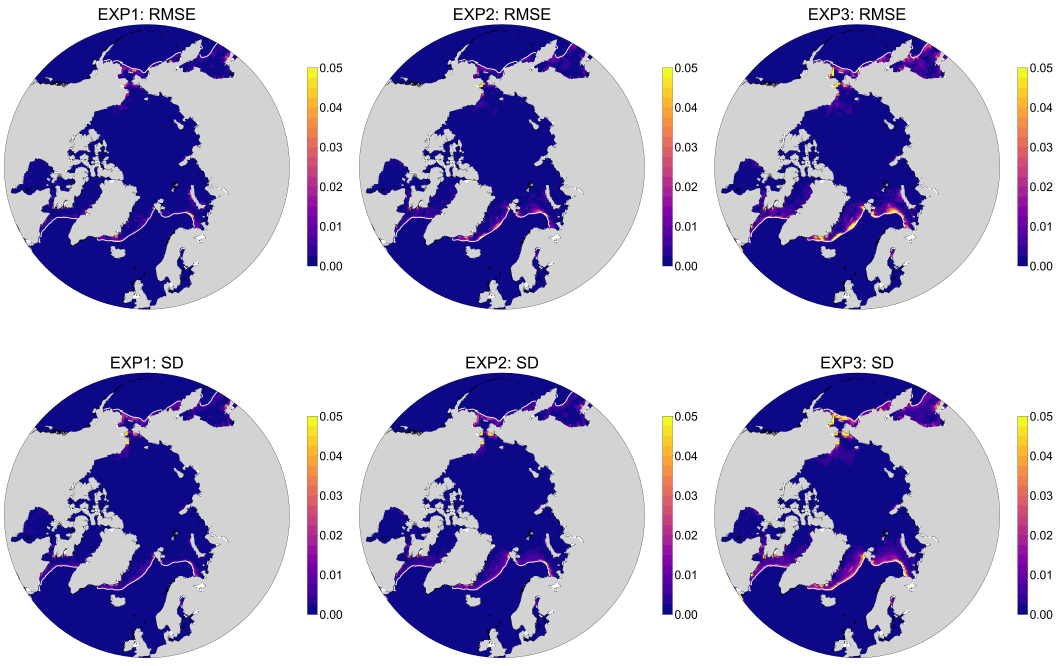

FIG. C1. As in Fig. 11 but for forecasts initialized on March 1st, 2019 for sea ice concentration.

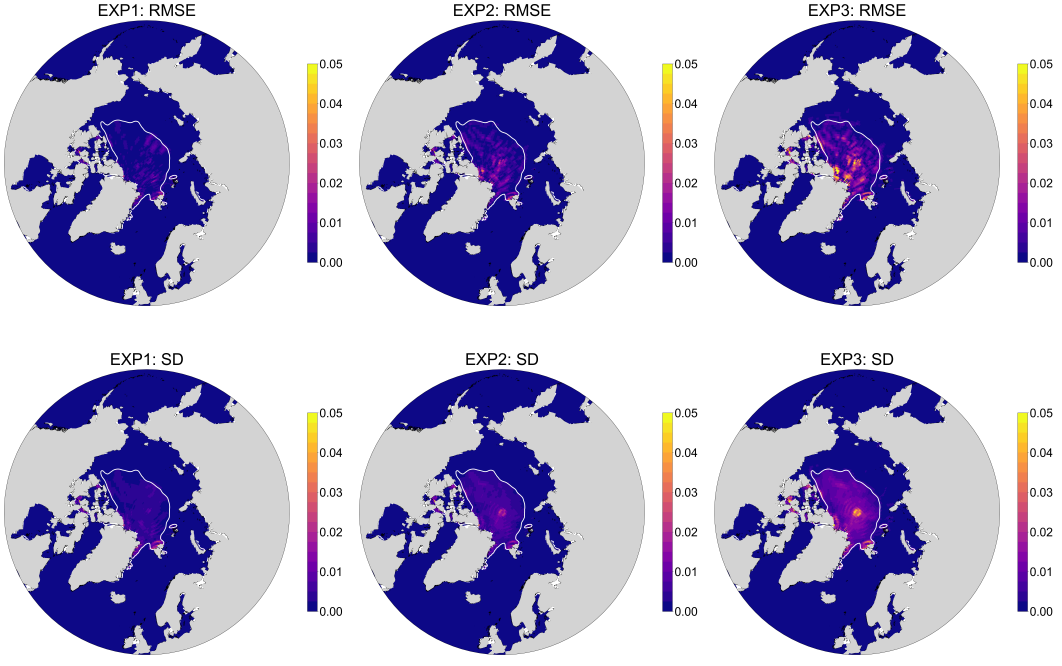

FIG. C2. As in Fig. 11 but for forecasts initialized on September 1st, 2019 for sea ice concentration.

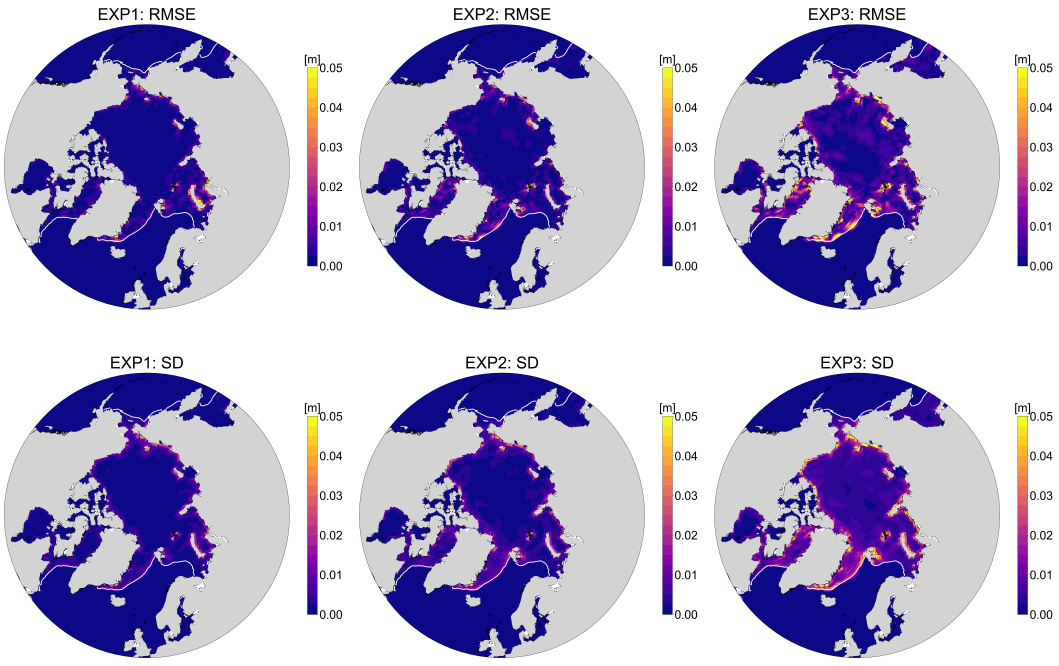

FIG. C3. As in Fig. 11 but for forecasts initialized on March 1st, 2019 for sea ice thickness.

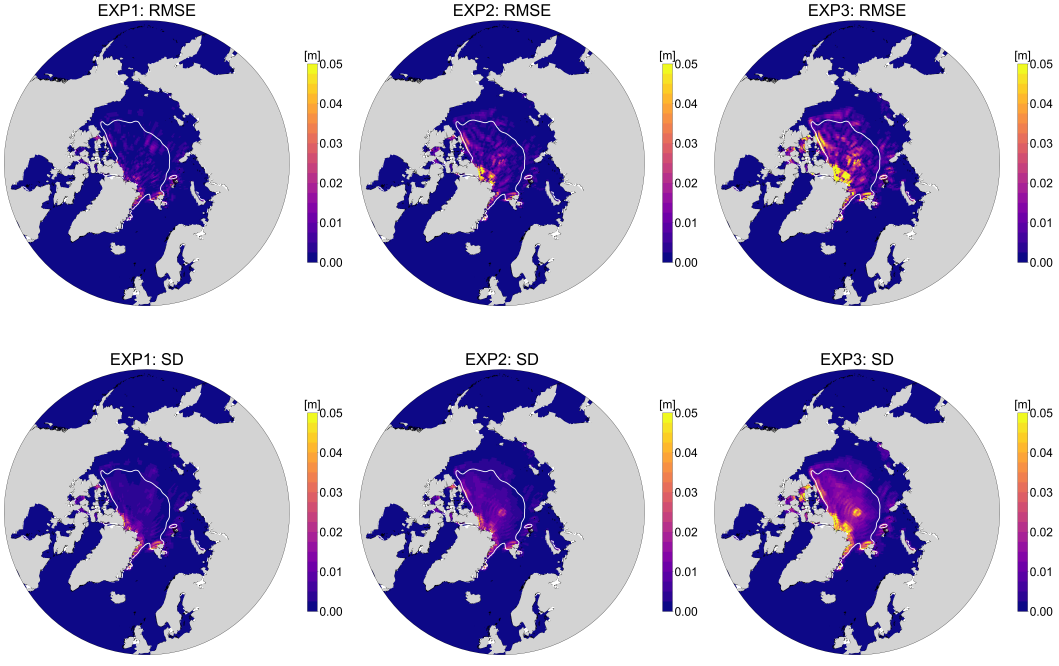

FIG. C4. As in Fig. 11 but for forecasts initialized on September 1st, 2019 for sea ice thickness.

References

Bannister, R. N., 2008: A review of forecast error covariance statistics in atmospheric variational data assimilation. I: Characteristics and measurements of forecast error covariances. https://doi.org/10.1002/qj.339.

Barton, N., and Coauthors, 2021: The Navy's Earth System Prediction Capability: A New Global Coupled Atmosphere-Ocean-Sea Ice Prediction System Designed for Daily to Subseasonal Forecasting. *Earth and Space Science*, **8 (4)**, https://doi.org/10.1029/2020EA001199.

Blayo, , M. Bocquet, E. Cosme, and L. F. Cugliandolo, 2014: *Advanced data assimilation for geosciences: Lecture notes of the LES Houches School of Physics: Special issue, June 2012*. OUP Oxford.

Brusdal, K., J. M. Brankart, G. Halberstadt, G. Evensen, P. Brasseur, P. J. Van Leeuwen, E. Dombrowsky, and J. Verron, 2003: A demonstration of ensemble-based assimilation methods with a layered OGCM from the perspective of operational ocean forecasting systems. *Journal of Marine Systems*, Vol. 40-41, https://doi.org/10.1016/S0924-7963(03)00021-6.

Cavallo, S. M., M. C. Frank, and C. M. Bitz, 2025: Sea ice loss in association with Arctic cyclones. *Communications Earth & Environment*, **6 (1)**, 44, https://doi.org/10.1038/s43247-025-02022-9.

Caya, A., M. Buehner, and T. Carrieres, 2010: Analysis and forecasting of sea ice conditions with three-dimensional variational data assimilation and a coupled ice-ocean model. *Journal of Atmospheric and Oceanic Technology*, **27 (2)**, https://doi.org/10.1175/2009JTECHO701.1.

Cheng, S., Y. Chen, A. Aydogdu, L. Bertino, A. Carrassi, P. Rampal, and C. K. Jones, 2023: Arctic sea ice data assimilation combining an ensemble Kalman filter with a novel Lagrangian sea ice model for the winter 2019-2020. *Cryosphere*, **17 (4)**, https://doi.org/10.5194/tc-17-1735-2023.

Croad, H. L., S. P. E. Keeley, J. Methven, B. Harvey, and A. Volonté, 2025: Examining the sensitivity of ECMWF IFS weather forecasts to sea-ice coupling for the summer-time Arctic and cyclones. *Quarterly Journal of the Royal Meteorological Society*, **151 (766)**, e4899, https://doi.org/https://doi.org/10.1002/qj.4899.

Danabasoglu, G., and Coauthors, 2020: The Community Earth System Model Version 2 (CESM2). *Journal of Advances in Modeling Earth Systems*, **12 (2)**, https://doi.org/10.1029/2019MS001916.

Data Assimilation Research Section Computational & Information Systems National Center for Atmospheric Research University Corporation for Atmospheric Research, 2020: CAM6 Data Assimilation Research Testbed (DART) Reanalysis. NSF National Center for Atmospheric Research, Boulder, CO, https://doi.org/10.5065/JG1E-8525.

Day, J. J., S. Keeley, G. Arduini, L. Magnusson, K. Mogensen, M. Rodwell, I. Sandu, and S. Tietsche, 2022: Benefits and challenges of dynamic sea ice for weather forecasts. *Weather and Climate Dynamics*, **3 (3)**, https://doi.org/10.5194/wcd-3-713-2022.

de Rosnay, P., and Coauthors, 2022: Coupled data assimilation at ECMWF: current status, challenges and future developments. *Quarterly Journal of the Royal Meteorological Society*, **148 (747)**, https://doi.org/10.1002/qj.4330.

Derber, J., and F. Bouttier, 1999: A reformulation of the background error covariance in the ECMWF global data assimilation system. *Tellus, Series A: Dynamic Meteorology and Oceanography*, **51 (2)**, https://doi.org/10.3402/tellusa.v51i2.12316.

Evensen, G., 2003: The Ensemble Kalman Filter: Theoretical formulation and practical implementation. *Ocean Dynamics*, **53 (4)**, https://doi.org/10.1007/s10236-003-0036-9.

Fiedler, E. K., M. J. Martin, E. Blockley, D. Mignac, N. Fournier, A. Ridout, A. Shepherd, and R. Tilling, 2022: Assimilation of sea ice thickness derived from CryoSat-2 along-track freeboard measurements into the Met Office's Forecast Ocean Assimilation Model (FOAM). *Cryosphere*, **16 (1)**, https://doi.org/10.5194/tc-16-61-2022.

Fisher, M., 2003: Background error covariance modelling. *Seminar on Recent Development in Data Assimilation . . . .*

Gharamti, M. E., and Coauthors, 2025: The Data Assimilation Research Testbed: A Robust, Scalable Software Facility with Groundbreaking Capabilities for Model-Data Integration. *Bulletin of the American Meteorological Society*, **106 (11)**, E2328 – E2345, https://doi.org/10.1175/BAMS-D-24-0214.1.

Goff, J. A., and S. Gratch, 1946: Low-pressure properties of water from –160 to 212 F. *Transactions of the American Society of Heating and Ventilating Engineers*, **52**.

Guemas, V., and Coauthors, 2016: A review on Arctic sea-ice predictability and prediction on seasonal to decadal time-scales. *Quarterly Journal of the Royal Meteorological Society*, **142 (695)**, https://doi.org/10.1002/qj.2401.

Harlim, J., and A. J. Majda, 2010: Catastrophic filter divergence in filtering nonlinear dissipative systems. *Communications in Mathematical Sciences*, **8 (1)**, https://doi.org/10.4310/CMS.2010.v8.n1.a3.

Holm, E., E. Andersson, A. Beljaars, and P. Lopez, 2002: Assimilation and modelling of the hydrological cycle: ECMWF's status and plans. *Technical Memorandum - ECMWF*, **(September)**.

Honda, Y., M. Nishijima, K. Koizumi, Y. Ohta, K. Tamiya, T. Kawabata, and T. Tsuyuki, 2006: A pre-operational variational data assimilation system for a non-hydrostatic model at the Japan Meteorological Agency: Formulation and preliminary results. *Quarterly Journal of the Royal Meteorological Society*, **131 (613)**, https://doi.org/10.1256/qj.05.132.

Hunke, E. C., W. H. Lipscomb, A. K. Turner, N. Jeffery, and S. Elliot, 2015: CICE : the Los Alamos Sea Ice Model Documentation and Software User's Manual Version 5.1 LA-CC-06-012. *Los Alamos National Laboratory Tech. Rep. LA-CC-06-012*, **(March 17)**.

Ingleby, N. B., A. C. Lorenc, K. Ngan, F. Rawlins, and D. R. Jackson, 2013: Improved variational analyses using a nonlinear humidity control variable. *Quarterly Journal of the Royal Meteorological Society*, **139 (676)**, https://doi.org/10.1002/qj.2073.

Jung, H.-S., 2026: Codes for "A State-Dependent Error Covariance
}Model of Surface Atmospheric Forcings over the
}Arctic Sea Ice"
}. Zenodo, URL https://doi.org/10.5281/zenodo.21014570, https://doi.org/10.5281/zenodo.21014570.

Kasahara, A., 1974: Various Vertical Coordinate Systems Used for Numerical Weather Prediction. *Monthly Weather Review*, **102 (7)**, https://doi.org/10.1175/1520-0493(1974)102⟨0509:vvcsuf⟩2.0.co;2.

Kay, J. E., and Coauthors, 2015: The community earth system model (CESM) large ensemble project : A community resource for studying climate change in the presence of internal climate variability. *Bulletin of the American Meteorological Society*, **96 (8)**, https://doi.org/10.1175/BAMS-D-13-00255.1.

Keeley, S., and K. Mogensen, 2018: Dynamic sea ice in the IFS. URL https://www.ecmwf.int/node/18874, 23–29 pp., https://doi.org/10.21957/4ska25furb.

Kousal, J., and Coauthors, 2025: Numerical Weather Prediction model coupling - strategies, challenges, and outlook. *Bulletin of the American Meteorological Society*, https://doi.org/10.1175/bams-d-25-0270.1.

Lee, J. G., and Y. G. Ham, 2022: Satellite-Based Data Assimilation System for the Initialization of Arctic Sea Ice Concentration and Thickness Using CICE5. *Frontiers in Climate*, **4**, https://doi.org/10.3389/fclim.2022.797733.

Leutbecher, M., and T. N. Palmer, 2008: Ensemble forecasting. *Journal of Computational Physics*, **227 (7)**, 3515–3539, https://doi.org/https://doi.org/10.1016/j.jcp.2007.02.014.

Li, L., N. Žagar, K. Raeder, and J. L. Anderson, 2023: Comparison of temperature and wind observations in the Tropics in a perfect-model, global EnKF data assimilation system. *Quarterly Journal of the Royal Meteorological Society*, **149 (755)**, https://doi.org/10.1002/qj.4511.

Lorenc, A. C., and Coauthors, 2000: The Met. Office global three-dimensional variational data assimilation scheme. *Quarterly Journal of the Royal Meteorological Society*, **126 (570)**, https://doi.org/10.1256/smsqj.57001.

Luo, H., Q. Yang, M. Mazloff, and D. Chen, 2023: A Balanced Atmospheric Ensemble Forcing for Sea Ice Modeling in Southern Ocean. *Geophysical Research Letters*, **50 (5)**, https://doi.org/10.1029/2022GL101139.

Mathiot, P., C. König Beatty, T. Fichefet, H. Goosse, F. Massonnet, and M. Vancoppenolle, 2012: Better constraints on the sea-ice state using global sea-ice data assimilation. *Geoscientific Model Development*, **5 (6)**, https://doi.org/10.5194/gmd-5-1501-2012.

McColl, K. A., and L. I. Tang, 2024: An Analytic Theory of Near-Surface Relative Humidity over Land. *Journal of Climate*, **37 (4)**, https://doi.org/10.1175/JCLI-D-23-0342.1.

Mignac, D., M. Martin, E. Fiedler, E. Blockley, and N. Fournier, 2022: Improving the Met Office's Forecast Ocean Assimilation Model (FOAM) with the assimilation of satellite-derived sea-ice thickness data from CryoSat-2 and SMOS in the Arctic. *Quarterly Journal of the Royal Meteorological Society*, **148 (744)**, https://doi.org/10.1002/qj.4252.

Mirouze, I., and A. Storto, 2019: Generating atmospheric forcing perturbations for an ocean data assimilation ensemble. *Tellus, Series A: Dynamic Meteorology and Oceanography*, **71 (1)**, https://doi.org/10.1080/16000870.2019.1624459.

Mohammadi-Aragh, M., H. F. Goessling, M. Losch, N. Hutter, and T. Jung, 2018: Predictability of Arctic sea ice on weather time scales. *Scientific Reports*, **8 (1)**, https://doi.org/10.1038/s41598-018-24660-0.

Palmer, T., R. Buizza, R. Hagedorn, A. Lawrence, M. Leutbecher, and L. Smith, 2006: Ensemble prediction: a pedagogical perspective. *ECMWF Newsletter*, **106 (106)**.

Parkinson, C. L., and J. C. Comiso, 2013: On the 2012 record low Arctic sea ice cover: Combined impact of preconditioning and an August storm. *Geophysical Research Letters*, **40 (7)**, 1356–1361, https://doi.org/https://doi.org/10.1002/grl.50349.

Parrish, D. F., and J. C. Derber, 1992: The National Meteorological Center's spectral statistical- interpolation analysis system. *Monthly Weather Review*, **120 (8)**, https://doi.org/10.1175/1520-0493(1992)120⟨1747:TNMCSS⟩2.0.CO;2.

Penny, S. G., E. Bach, K. Bhargava, C. C. Chang, C. Da, L. Sun, and T. Yoshida, 2019: Strongly Coupled Data Assimilation in Multiscale Media: Experiments Using a Quasi-Geostrophic Coupled Model. *Journal of Advances in Modeling Earth Systems*, **11 (6)**, https://doi.org/10.1029/2019MS001652.

Peterson, K. A., and Coauthors, 2022: Understanding sources of Northern Hemisphere uncertainty and forecast error in a medium-range coupled ensemble sea-ice prediction system. *Quarterly Journal of the Royal Meteorological Society*, **148 (747)**, https://doi.org/10.1002/qj.4340.

Petty, G. W., 2006: *A First Course in Atmospheric Radiation*. Sundog Publishing, URL https://books.google.com/books?id=2bPlEAAAQBAJ.

Phillips, N. A., 1957: A COORDINATE SYSTEM HAVING SOME SPECIAL ADVANTAGES FOR NUMERICAL FORECASTING. *Journal of Meteorology*, **14 (2)**, https://doi.org/10.1175/1520-0469(1957)014⟨0184:acshss⟩2.0.co;2.

Purser, R. J., W. S. Wu, D. F. Parrish, and N. M. Roberts, 2003a: Numerical aspects of the application of recursive filters to variational statistical analysis. Part I: Spatially homogeneous and isotropic Gaussian covariances. *Monthly Weather Review*, **131 (8 PART 1)**, https://doi.org/10.1175//1520-0493(2003)131⟨1524:NAOTAO⟩2.0.CO;2.

Purser, R. J., W. S. Wu, D. F. Parrish, and N. M. Roberts, 2003b: Numerical aspects of the application of recursive filters to variational statistical analysis. Part II: Spatially inhomogeneous and anisotropic general covariances. *Monthly Weather Review*, **131 (8 PART 1)**, https://doi.org/10.1175//2543.1.

Raeder, K., T. J. Hoar, M. El Gharamti, B. K. Johnson, N. Collins, J. L. Anderson, J. Steward, and M. Coady, 2021: A new CAM6 + DART reanalysis with surface forcing from CAM6 to other CESM models. *Scientific Reports*, **11 (1)**, https://doi.org/10.1038/s41598-021-92927-0.

Raymond, W. H., 2000: Moisture Advection Using Relative Humidity. *Journal of Applied Meteorology*, **39 (12 PART 2)**, https://doi.org/10.1175/1520-0450(2000)039⟨2397:maurh⟩2.0.co;2.

Riedel, C., and J. Anderson, 2024: Exploring non-Gaussian sea ice characteristics via observing system simulation experiments. *The Cryosphere*, **18 (6)**, 2875–2896, https://doi.org/10.5194/tc-18-2875-2024.

Riedel, C. P., M. M. Wieringa, and J. L. Anderson, 2025: Exploring Bounded Nonparametric Ensemble Filter Impacts on Sea Ice Data Assimilation. *Monthly Weather Review*, **153 (4)**, 637 – 654, https://doi.org/10.1175/MWR-D-24-0096.1.

Rodwell, M. J., S. T. Lang, N. B. Ingleby, N. Bormann, E. Hólm, F. Rabier, D. S. Richardson, and M. Yamaguchi, 2016: Reliability in ensemble data assimilation. *Quarterly Journal of the Royal Meteorological Society*, **142 (694)**, https://doi.org/10.1002/qj.2663.

Schüller, V., F. Lemarié, P. Birken, and E. Blayo, 2025: Quantifying coupling errors in atmosphere-ocean-sea ice models: A study of iterative and non-iterative approaches in the EC-Earth AOSCM. *Geoscientific Model Development*, **18 (22)**, https://doi.org/10.5194/gmd-18-9167-2025.

Shakespeare, C. J., and M. L. Roderick, 2024: What Controls Near-Surface Relative Humidity Over the Ocean? *Journal of Advances in Modeling Earth Systems*, **16 (6)**, https://doi.org/10.1029/2023MS004168.

Simpson, I. R., and Coauthors, 2023: The CESM2 Single-Forcing Large Ensemble and Comparison to CESM1: Implications for Experimental Design. *Journal of Climate*, **36 (17)**, https://doi.org/10.1175/JCLI-D-22-0666.1.

Stull, R. B., 1988: An introduction to boundary layer meteorology. *An introduction to boundary layer meteorology*, https://doi.org/10.1007/978-94-009-3027-8.

Tang, Q., L. Mu, H. F. Goessling, T. Semmler, and L. Nerger, 2021: Strongly Coupled Data Assimilation of Ocean Observations Into an Ocean-Atmosphere Model. *Geophysical Research Letters*, **48 (24)**, https://doi.org/10.1029/2021GL094941.

Tian, T., S. Yang, M. P. Karami, F. Massonnet, T. Kruschke, and T. Koenigk, 2021: Benefits of sea ice initialization for the interannual-to-decadal climate prediction skill in the Arctic in EC-Earth3. *Geoscientific Model Development*, **14 (7)**, https://doi.org/10.5194/gmd-14-4283-2021.

Turner, M. R., J. P. Walker, and P. R. Oke, 2008: Ensemble member generation for sequential data assimilation. *Remote Sensing of Environment*, **112 (4)**, https://doi.org/10.1016/j.rse.2007.02.042.

Valmassoi, A., and Coauthors, 2023: Current Challenges and Future Directions in Data Assimilation and Reanalysis. *Bulletin of the American Meteorological Society*, **104 (4)**, https://doi.org/10.1175/BAMS-D-21-0331.1.

Wang, Z., J. Walsh, S. Szymborski, and M. Peng, 2020: Rapid arctic sea ice loss on the synoptic time scale and related atmospheric circulation anomalies. *Journal of Climate*, **33 (5)**, https://doi.org/10.1175/JCLI-D-19-0528.1.

Weaver, A. T., C. Deltel, E. Machu, S. Ricci, and N. Daget, 2006: A multivariate balance operator for variational ocean data assimilation. *Quarterly Journal of the Royal Meteorological Society*, **131 (613)**, https://doi.org/10.1256/qj.05.119.

Wieringa, M. M., C. Riedel, J. L. Anderson, and C. M. Bitz, 2024: Bounded and categorized: targeting data assimilation for sea ice fractional coverage and nonnegative quantities in a single-

column multi-category sea ice model. *The Cryosphere*, **18 (11)**, 5365–5382, https://doi.org/10.5194/tc-18-5365-2024.

Williams, N., N. Byrne, D. Feltham, P. J. Van Leeuwen, R. Bannister, D. Schroeder, A. Ridout, and L. Nerger, 2023: The effects of assimilating a sub-grid-scale sea ice thickness distribution in a new Arctic sea ice data assimilation system. *Cryosphere*, **17 (6)**, https://doi.org/10.5194/tc-17-2509-2023.

Wu, W. S., R. J. Purser, and D. F. Parrish, 2002: Three-dimensional variational analysis with spatially inhomogeneous covariances. *Monthly Weather Review*, **130 (12)**, https://doi.org/10.1175/1520-0493(2002)130⟨2905:TDVAWS⟩2.0.CO;2.

Xie, J., Y. Ying, R. Davy, and L. Bertino, 2026: Impact of data assimilation on Arctic sea-ice thickness variability and its coupling with atmospheric forcing. *Quarterly Journal of the Royal Meteorological Society*, **n/a (n/a)**, e70 210, https://doi.org/https://doi.org/10.1002/qj.70210.

Yang, Q., S. N. Losa, M. Losch, T. Jung, and L. Nerger, 2015: The role of atmospheric uncertainty in Arctic summer sea ice data assimilation and prediction. *Quarterly Journal of the Royal Meteorological Society*, **141 (691)**, https://doi.org/10.1002/qj.2523.

Zhang, Y. F., C. M. Bitz, J. L. Anderson, N. Collins, J. Hendricks, T. Hoar, K. Raeder, and F. Massonnet, 2018: Insights on Sea Ice data assimilation from perfect model observing system simulation experiments. *Journal of Climate*, **31 (15)**, https://doi.org/10.1175/JCLI-D-17-0904.1.

Zhang, Y. F., M. Bushuk, M. Winton, B. Hurlin, X. Yang, T. Delworth, and L. Jia, 2021: Assimilation of satellite-retrieved sea ice concentration and prospects for september predictions of arctic sea ice. *Journal of Climate*, **34 (6)**, https://doi.org/10.1175/JCLI-D-20-0469.1.

Zheng, F., and J. Zhu, 2008: Balanced multivariate model errors of an intermediate coupled model for ensemble Kalman filter data assimilation. *Journal of Geophysical Research: Oceans*, **113 (7)**, https://doi.org/10.1029/2007JC004621.